

# UC Davis

## UC Davis Previously Published Works

### Title

$\alpha$ -Actinin-1 promotes activity of the L-type Ca<sup>2+</sup> channel Cav1.2

### Permalink

<https://escholarship.org/uc/item/9jk7j0kq>

### Journal

The EMBO Journal, 39(5)

### ISSN

0261-4189

### Authors

Turner, Matthew  
Anderson, David E  
Bartels, Peter  
[et al.](#)

### Publication Date










2020-03-02

### DOI

10.15252/emj.2019102622

Peer reviewed

# $\alpha$ -Actinin-1 promotes activity of the L-type $\text{Ca}^{2+}$ channel $\text{Ca}_v1.2$

Matthew Turner<sup>1,†</sup>, David E Anderson<sup>1,†</sup>, Peter Bartels<sup>2,†</sup> , Madeline Nieves-Cintron<sup>2,†</sup> ,  
Andrea M Coleman<sup>1,2</sup> , Peter B Henderson<sup>2</sup>, Kwun Nok Mimi Man<sup>2</sup> , Pang-Yen Tseng<sup>2</sup>,  
Vladimir Yarov-Yarovoy<sup>3</sup> , Donald M Bers<sup>2</sup>, Manuel F Navedo<sup>2</sup> , Mary C Horne<sup>2,\*</sup> ,  
James B Ames<sup>1,\*\*</sup>  & Johannes W Hell<sup>2,\*\*\*</sup> 

## Abstract

The L-type  $\text{Ca}^{2+}$  channel  $\text{Ca}_v1.2$  governs gene expression, cardiac contraction, and neuronal activity. Binding of  $\alpha$ -actinin to the IQ motif of  $\text{Ca}_v1.2$  supports its surface localization and postsynaptic targeting in neurons. We report a bi-functional mechanism that restricts  $\text{Ca}_v1.2$  activity to its target sites. We solved separate NMR structures of the IQ motif (residues 1,646–1,664) bound to  $\alpha$ -actinin-1 and to apo-calmodulin (apoCaM). The  $\text{Ca}_v1.2$  K1647A and Y1649A mutations, which impair  $\alpha$ -actinin-1 but not apoCaM binding, but not the F1658A and K1662E mutations, which impair apoCaM but not  $\alpha$ -actinin-1 binding, decreased single-channel open probability, gating charge movement, and its coupling to channel opening. Thus,  $\alpha$ -actinin recruits  $\text{Ca}_v1.2$  to defined surface regions and simultaneously boosts its open probability so that  $\text{Ca}_v1.2$  is mostly active when appropriately localized.

**Keywords** calmodulin; gating charge; IQ motif structure; open probability; surface expression

**Subject Categories** Membranes & Trafficking; Neuroscience

**DOI** 10.15252/emj.2019102622 | Received 5 June 2019 | Revised 4 December 2019 | Accepted 6 December 2019 | Published online 27 January 2020

**The EMBO Journal (2020) 39: e102622**

## Introduction

$\text{Ca}^{2+}$  influx through  $\text{Ca}_v1.2$  is critical for the functions of many organs as strikingly illustrated by Timothy syndrome (Splawski *et al*, 2004). In this disease, a point mutation in  $\text{Ca}_v1.2$  causes, among other symptoms, lethal arrhythmias, autistic-like behaviors, immune deficiency, and webbing of fingers (Splawski *et al*, 2004).  $\text{Ca}_v1.2$  is the main L-type channel in heart (Seisenberger *et al*, 2000), vascular smooth muscle cells (Ghosh *et al*, 2017), and brain

(Hell *et al*, 1993; Sinnegger-Brauns *et al*, 2004).  $\text{Ca}^{2+}$  influx through  $\text{Ca}_v1.2$  triggers cardiac contraction, regulates arterial tone (Ghosh *et al*, 2017), mediates different forms of synaptic long-term potentiation (Grover & Teyler, 1990; Patriarchi *et al*, 2016; Qian *et al*, 2017), and controls neuronal excitability (Marrion & Tavalin, 1998; Berkefeld *et al*, 2006). Furthermore, L-type channels are much more strongly coupled to gene expression than other  $\text{Ca}^{2+}$  channels (Dolmetsch *et al*, 2001; Li *et al*, 2012; Ma *et al*, 2014; Cohen *et al*, 2018). Finally,  $\text{Ca}_v1.2$  forms a physical and functional complex with the  $\beta_2$  adrenergic receptor (Davare *et al*, 2001) making it a prime target for signaling by norepinephrine (Patriarchi *et al*, 2016; Qian *et al*, 2017; Man *et al*, 2020), which is important for wakefulness, attention, and various forms of learning (Cahill *et al*, 1994; Berman & Dudai, 2001; Hu *et al*, 2007; Minzenberg *et al*, 2008; Carter *et al*, 2010).

$\text{Ca}_v1.2$  consists of the pore-forming  $\alpha_11.2$  subunit and auxiliary  $\alpha_2\delta$  and  $\beta$  subunits, which facilitate release from the endoplasmic reticulum and the controlled trafficking of  $\text{Ca}_v1.2$  to the cell surface (Dai *et al*, 2009; Dolphin, 2012, 2016; Zamponi *et al*, 2015; Ghosh *et al*, 2018). However,  $\alpha_2\delta$  and  $\beta$  subunits do not target  $\text{Ca}_v1.2$  to specific sites in the plasma membrane. Rather,  $\text{Ca}_v1.2$  anchoring at defined regions at the cell surface is mediated by  $\alpha$ -actinin, which binds to the IQ motif in the C-terminus of  $\alpha_11.2$  (Hall *et al*, 2013; Tseng *et al*, 2017).

A systematic yeast two-hybrid screen defined three residues in the IQ motif of  $\alpha_11.2$ , whose mutations to alanine residues affect  $\alpha$ -actinin binding: K1647A, Y1649A, and I1654A. All three mutations reduced surface expression of  $\text{Ca}_v1.2$  by ~35% but current density by 70–80% (Tseng *et al*, 2017). These results suggest that  $\alpha$ -actinin binding to the IQ motif promotes not only surface localization but also channel activity. Such a multifunctional role would ensure that  $\text{Ca}_v1.2$  is mostly active at its ultimate destinations and much less so when in transit and outside its target areas.

1 Department of Chemistry, University of California, Davis, CA, USA

2 Department of Pharmacology, University of California, Davis, CA, USA

3 Department of Physiology and Membrane Biology, University of California, Davis, CA, USA

\*Corresponding author. Tel: +1 530 752 7723; E-mail: mhorne@ucdavis.edu

\*\*Corresponding author. Tel: +1 530 752 6358; E-mail: jbames@ucdavis.edu

\*\*\*Corresponding author. Tel: +1 530 752 6540; E-mail: jwhell@ucdavis.edu

†These authors contributed equally to this work

The closely related  $\alpha_1$ 1.3 subunit of the L-type channel  $\text{Ca}_v$ 1.3 shares nearly 100% sequence identity with  $\alpha_1$ 1.2 in its membrane-proximal 165 residues of its C-terminus in which the IQ motif is embedded (the eponymous Ile is I1654 of  $\alpha_1$ 1.2 and I1609 of  $\alpha_1$ 1.3; Appendix Fig S1).  $\text{Ca}^{2+}$ -free calmodulin (apoCaM) binds to this IQ motif, and mutation of I1609 in  $\alpha_1$ 1.3 impairs both, apoCaM binding and open probability  $P_o$  of  $\text{Ca}_v$ 1.3 (Ben Johny *et al*, 2013; Adams *et al*, 2014; Ben-Johny *et al*, 2014). We solved the NMR structures of the third and fourth EF hands of  $\alpha$ -actinin-1 (EF3 and EF4, residues 822–892; Fig 1A) and of full-length apoCaM bound to the  $\alpha$ -helical IQ motif of  $\text{Ca}_v$ 1.2 (residues 1,646–1,664). This work provided new insight into the structure of  $\text{Ca}_v$ 1.2 especially as relevant for these two critical binding partners and informed experiments that dissected the exact functions of  $\alpha$ -actinin versus apoCaM binding. Refined analysis of  $\text{Ca}_v$ 1.2 activity by cell-attached single-channel recording revealed that point mutations that affected  $\alpha$ -actinin-1 but not those that affected apoCaM binding dramatically decreased the channel  $P_o$  by impairing gating charge movement as well as its coupling to channel opening. We conclude that  $\alpha$ -actinin plays a dual role by anchoring  $\text{Ca}_v$ 1.2 at specific subcellular domains such as the postsynaptic sites and at the same time boosting its open probability. This mechanism ensures that the activity of  $\text{Ca}_v$ 1.2 is minimal when in transit during secretory trafficking and outside its intended location at the cell surface, where its  $\text{Ca}^{2+}$  conductance could adversely affect cell functions, but maximal at its final destination.

## Results

### Binding of $\alpha$ -actinin-1 EF3/EF4 to the $\text{Ca}_v$ 1.2 IQ motif

$\alpha$ -actinin is encoded by four homologous genes with  $\alpha$ -actinin-1 and  $\alpha$ -actinin-2 being most prominent in neurons (Wyszynski *et al*, 1997; Hall *et al*, 2013; Hell, 2014; Matt *et al*, 2018).  $\alpha$ -actinins consist of two N-terminal calponin homology domains (CH1, CH2; residues 19–192), four central spectrin repeats (SR1–4), which form a rod-like coiled-coil structure (Ribeiro Ede *et al*, 2014), and four EF hands at their C-termini (residues 750–892; Fig 1A). We first performed NMR spectroscopy with the CH1/CH2 region (residues 19–192). Two-dimensional NMR spectra of  $^{15}\text{N}$ -labeled CH1/CH2 recorded in the presence and absence of unlabeled IQ peptide appeared to be virtually identical, consistent with a lack of IQ binding to CH1/CH2 under NMR conditions (Fig EV1A). The lack of IQ binding to the CH1/CH2 domain is supported by the absence of detectable binding measured by fluorescence polarization (see below Fig 1F). In stark contrast, the NMR spectrum of  $^{15}\text{N}$ -labeled EF-hand domain of  $\alpha$ -actinin-1 (residues 750–892) showed clearly detectable spectral changes upon adding a saturating amount of unlabeled IQ peptide, demonstrating a binding interaction (Fig EV1B). The NMR peaks of  $\alpha$ -actinin-1 most affected by the binding of IQ (see labeled peaks in Fig EV1B) were assigned to residues in EF3 and EF4 (the C-lobe of the EF-hand region; residues 822–892). Consistently, the NMR spectrum of  $^{15}\text{N}$ -labeled  $\alpha$ -actinin-1 EF3/4 (residues 822–892) exhibited large spectral changes upon the addition of the IQ peptide (Fig EV1C), which are similar to those seen with the construct that contains all four EF hands (Fig EV1B). We conclude that the IQ peptide binds to the  $\alpha$ -actinin-1 C-lobe.

### NMR structure of $\alpha$ -actinin-1 EF3/4 bound to the IQ motif of $\text{Ca}_v$ 1.2

We had previously reported NMR spectral assignments for  $\alpha$ -actinin-1 EF3/4 (BMRB accession number 25902) (Turner *et al*, 2016). We used these assignments to obtain NMR-derived structural restraints for high-resolution structural analysis of  $\alpha$ -actinin-1 EF3/4 bound to the  $\text{Ca}_v$ 1.2 IQ motif (EF3/4-IQ). Atomic-level NMR structures were calculated on the basis of distance restraints derived from the analysis of NOESY spectra and long-range orientational restraints derived from residual dipolar coupling (RDC) data (Fig EV2A). EF34 in the complex was resolved for 69 residues, starting at T823 and ending at L892. The 10 lowest energy NMR structures are overlaid in Fig 1B and structural statistics summarized in Table 1. The overall precision of the ensemble was expressed by an RMSD of 0.3 Å calculated from the coordinates of the main chain atoms. The energy-minimized average structure of EF3/4-IQ (Fig 1C, calculated from the ensembles in Fig 1B) contained two EF-hand motifs ( $\alpha$ 1: A826–A837;  $\alpha$ 2: M845–E851;  $\alpha$ 3: P854–R863;  $\alpha$ 4: M880–Y887;  $\beta$ 1: Y842–T844;  $\beta$ 2: A876–D878) bound to an  $\alpha$ -helical IQ motif ( $\text{Ca}_v$ 1.2 residues 1,646–1,664). The NMR structure of EF3/4-IQ (Fig 1C) was quite similar (1.8 Å RMSD) to the NMR structure of  $\alpha$ -actinin-2 bound to the seventh Z-repeat of titin (Atkinson *et al*, 2001). It contained important intermolecular contacts that stabilize the EF3/4–IQ interaction (Fig 1C–E). Most striking were a salt bridge between IQ K1647 and EF3/4 E847/E851 (Fig 1C) and hydrophobic contacts involving IQ I1654 and EF3F833 (Fig 1D). The IQ residue F1658 was mostly solvent exposed in the EF3/4–IQ complex contributing minimally if at all to the EF3/4–IQ interaction (Fig 1E), in contrast to being buried inside apoCaM in the apoCaM/IQ complex (see below).

### Validation of the $\alpha$ -actinin-1 EF3/4–IQ NMR structure by mutagenesis

Mutations in both  $\alpha$ -actinin-1 EF3/4 and IQ peptide were designed to verify their predicted intermolecular contacts. A synthetic fluorescein-labeled IQ peptide (residues 1,644–1,666) was titrated with EF3/4 and fluorescence polarization (FP) monitored to determine their  $K_d$  values. The IQ peptide bound to  $\alpha$ -actinin-1 EF3/4 with nearly the same affinity as to full-length  $\alpha$ -actinin-1 (Fig 1F; Table 2). The IQ peptide did not bind to  $\alpha$ -actinin-1 EF1/2 (Fig 1F). Accordingly, IQ interacts exclusively with the C-lobe but not N-lobe of the EF-hand domain in  $\alpha$ -actinin-1.

The salt bridges formed between IQ residue K1647 and  $\alpha$ -actinin-1 residues E847 and E851 (Fig 1C) provided an opportunity for charge inversion experiments. The single-residue alterations K1647A and K1647E in the IQ peptide increased the  $K_d$  by ~5-fold and mutating E847 and E851 in  $\alpha$ -actinin-1 EF3/4 to lysine (K) by ~12-fold (Fig 1F; Table 2). Combining the E847K/E851K mutations in  $\alpha$ -actinin-1 EF3/4 with the K1647E substitution in the IQ peptide mostly but not fully restored the binding affinity to the K1647E IQ peptide. This powerful charge inversion experiment unequivocally identified the importance of those salt bridges for the  $\alpha$ -actinin-1–IQ interaction. Furthermore, I1654 of the IQ motif was predicted to form hydrophobic interactions with F833 in EF3 (Fig 1D). In fact, the  $\alpha$ -actinin-1 EF3/4 mutant F833A showed an ~8-fold decrease in binding affinity, which is consistent with the decrease observed for

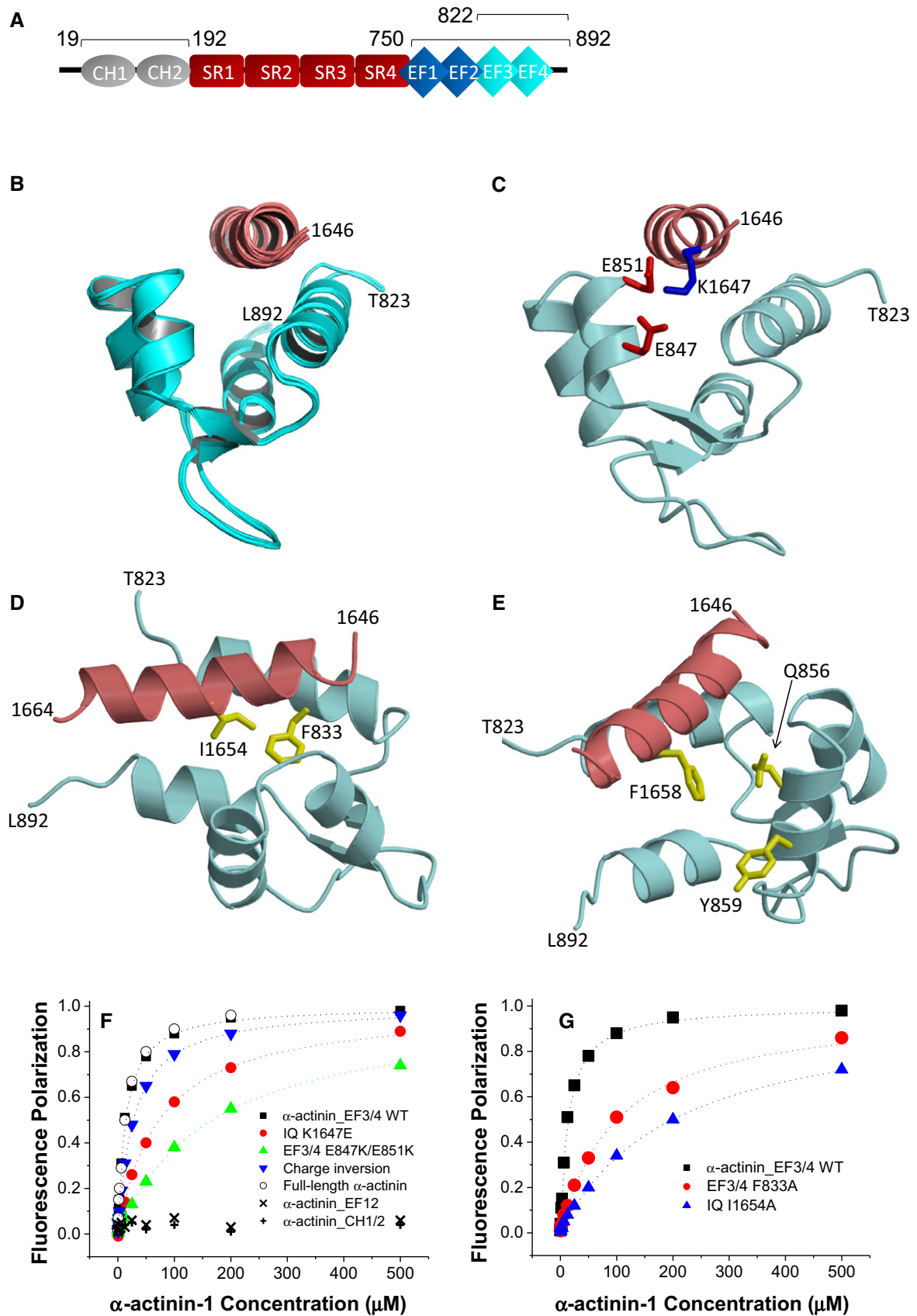


Figure 1.

**Figure 1.  $\alpha$ -Actinin-1 forms electrostatic and hydrophobic contacts with  $\text{Ca}_v1.2$ .**

- A Linear model of  $\alpha$ -actinin domains (CH: calponin homology domains; SR: spectrin repeats; EF: EF hands). Bars and numbers on top of the model depict the segments used in this work.
- B Ensemble of 10 lowest energy NMR-derived structures of  $\alpha$ -actinin-1\_EF34 (cyan) bound to IQ peptide (red). Structural statistics are given in Table 1.
- C Energy-minimized average structure of  $\alpha$ -actinin-1\_EF34 (cyan) bound to IQ (red), revealing intermolecular salt bridges between K1647 of IQ and E847/E851 of  $\alpha$ -actinin-1. The K1647 side-chain amino nitrogen atom is 2.8 and 2.5 Å away from the side-chain carbonyl oxygen atoms of E847 and E851, respectively.
- D Intermolecular hydrophobic contacts between I1654 of IQ (red) and F833 of  $\alpha$ -actinin-1 (cyan). The I1654 side-chain methyl carbon atom is 2.9 Å away from the closest aromatic ring atom of F833. Side-chain atoms are colored yellow.
- E Lack of direct contacts between F1658 of IQ (red) and  $\alpha$ -actinin-1 (cyan). The aromatic side chain of F1658 is primarily solvent exposed and does not directly contact  $\alpha$ -actinin-1. The aromatic ring of F1658 is closest to the aromatic ring of Y859 and  $\beta$ -methylene carbon of Q856 of  $\alpha$ -actinin-1, which are 5.2 and 4.3 Å apart, respectively.
- F FP titrations show binding of WT  $\alpha$ -actinin-1\_EF34 to IQ peptides WT (black) and K1647E (red), of  $\alpha$ -actinin-1\_EF34 mutant E847K/E851K to IQ peptides WT (green) and K1647E (blue), of full-length  $\alpha$ -actinin-1 to IQ WT (o), and lack of IQ binding to  $\alpha$ -actinin-1\_CH1-CH2 (+) and  $\alpha$ -actinin-1\_EF12 (x; see Table 2 for binding parameters and standard errors).
- G FP titrations showing binding of wild-type  $\alpha$ -actinin-1\_EF34 to IQ peptides WT (black) and I1654A (blue) and of ACTN1\_EF34 mutant F833 to IQ WT (red; see Table 2 for binding parameters and standard errors).

the I1654A substitution in the IQ peptide (Fig 1G; Table 2). These results confirmed two important intermolecular interactions that had been seen in the NMR structure (Fig 1C): a salt bridge contact between K1647 ( $\text{Ca}_v1.2$ ) and E847/E851 ( $\alpha$ -actinin-1) and the linchpin hydrophobic contact between I1654 ( $\text{Ca}_v1.2$ ) and F833 ( $\alpha$ -actinin-1).

**NMR structure of apoCaM bound to the IQ motif of  $\text{Ca}_v1.2$** 

ApoCaM is predicted to bind to the IQ motif of  $\text{Ca}_v1.3$  under basal conditions to augment  $\text{Po}$  (Adams *et al*, 2014) but no structure has so far been available to aid data interpretation. The  $^1\text{H}$ - $^{15}\text{N}$  HSQC NMR spectrum of  $^{15}\text{N}$ -labeled apoCaM showed detectable spectral changes upon adding a saturating amount of unlabeled IQ peptide, demonstrating binding (Fig EV1D). The NMR peaks of apoCaM most affected by the binding of IQ (see labeled peaks in Fig EV1D) were assigned to residues in its C-lobe (CaM EF3/4). Complete NMR

spectral assignments for apoCaM bound to the IQ peptide had been reported previously (Lian *et al*, 2007). We used these assignments to obtain NMR-derived structural restraints and determine the atomic-level NMR structure of apoCaM bound to the IQ peptide (called apoCaM-IQ). NMR-derived structures were calculated on the basis of NOESY distance restraints and long-range orientational restraints derived from NMR RDC data (Fig EV2B) (Tjandra & Bax, 1997). Our NMR chemical shift analysis indicated that the IQ peptide contacted residues in the C-lobe (residues 82–148) but not N-lobe of apoCaM (residues 1–78; Fig 2). The 10 lowest energy NMR structures are overlaid in Fig 2A and structural statistics summarized in Table 3. The overall precision of the ensemble was expressed by an RMSD of 0.6 Å calculated from the coordinates of the main chain atoms. The energy-minimized average structure of apoCaM/IQ (Fig 2B, calculated from the ensembles in Fig 2A) contained two EF-hand motifs (EF3 and EF4) in a semi-open conformation akin to that observed for apoCaM bound to the IQ motif in voltage-gated  $\text{Na}^+$  channels (Chagot & Chazin, 2011; Feldkamp *et al*, 2011). This semi-open apoCaM C-lobe structure was bound to the  $\alpha$ -helical IQ motif ( $\alpha_11.2$  residues 1,646–1,665; Fig 2B) with an orientation that was opposite to that observed in the crystal structure of  $\text{Ca}^{2+}$ -CaM bound to IQ (Van Petegem *et al*, 2005).

The NMR-derived structure of apoCaM bound to  $\alpha_11.2$  IQ peptide contained a number of important intermolecular contacts that

**Table 1. NMR structural statistics for  $\alpha$ -actinin-1 EF34/IQ.**

NMR structural restraints	
Intermolecular NOEs	73
Hydrogen bonds	62
RDC Q-Factor	0.095
$^3\text{D}_{\text{HN}}\text{RDC}$	34
RDC correlation coefficient (R)	0.99
Root mean squared deviation from average structure	
$\alpha$ -actinin-1 backbone atoms	0.5 Å $\pm$ 0.3 for 200 structures
$\alpha$ -actinin-1 backbone atoms (refined)	0.3 Å $\pm$ 0.2 for 50 structures
Haddock scoring	
Cluster size	194
Van der Waals energy	-40.2 $\pm$ 6.2
Electrostatic energy	-395.4 $\pm$ 37.1
Restraints violation energy	278.0 $\pm$ 6.23
Ramachandran plot	
Most favored regions	96.7%
Allowed regions	2.2%
Unfavored regions	1.1%

**Table 2.  $K_d$  (in  $\mu\text{M}$ ) for  $\alpha$ -actinin-1 EF3/EF4 binding to IQ as determined by FP.**

	$\alpha$ -actinin-1 EF3/4		
	WT	E847K/E851K	F833A
Ca <sub>v</sub> 1.2 IQ			
WT	14 $\pm$ 2	167 $\pm$ 20	100 $\pm$ 10
K1647E	73 $\pm$ 10	27 $\pm$ 2	/
K1647A	67 $\pm$ 10	/	/
Y1649A	42 $\pm$ 4	/	/
I1654A	200 $\pm$ 20	/	/
F1658A	20 $\pm$ 2	/	/
K1662E	20 $\pm$ 2	150 $\pm$ 20	/

Shown are mean  $\pm$  SD ( $n = 3$  for all conditions).



stabilized this interaction (Fig 2B–D). The most striking intermolecular interactions were as follows: (i) a salt bridge between IQ residue K1662 and apoCaM residue E88 (Fig 2B); (ii) hydrophobic contacts involving the side-chain atoms of IQ residue I1654 and apoCaM residue F90 (Fig 2C); and (iii) hydrophobic contacts involving the side-chain atoms of IQ residue F1658 and apoCaM residues F90/M110 (Fig 2D).

### Validation of the apoCaM–IQ NMR structure by mutagenesis

Mutations in both apoCaM and IQ peptide were introduced to verify their predicted intermolecular contacts. We titrated fluorescein-labeled IQ peptide (residues 1,644–1,666) with apoCaM and measured FP. The  $K_d$  for WT IQ peptide was 10  $\mu$ M (Fig 2E, Table 4), similar to the  $K_d$  of 13  $\mu$ M in earlier work (Evans *et al*, 2011). To understand why this  $K_d$  is ~20-fold higher than the  $K_d$  of 580 nM deducted previously from isothermal titration calorimetry (ITC) measurements (Findeisen *et al*, 2013), we performed ITC experiments by adding increments of apoCaM (100  $\mu$ M) to the IQ peptide (10  $\mu$ M) under near physiological salt concentration (100 mM KCl, Appendix Fig S2A). No heat signal other than that of dilution was detectable (Appendix Fig S2B). The prior ITC experiments were performed at 5 mM KCl (Findeisen *et al*, 2013) and may represent a non-physiological electrostatic attraction between oppositely charged apoCaM and IQ that is suppressed by more physiological salt levels (100 mM KCl). Indeed, apoCaM binds to the IQ peptide with nearly fourfold higher affinity in the absence of salt (Appendix Fig S2C;  $K_d$  is 2.6  $\mu$ M at 0 KCl and 10  $\mu$ M at 100 mM KCl).

According to our FP-binding assay, the K1662E mutation in the IQ peptide and the E88K mutation in apoCaM each decreased the binding affinity between IQ peptide and apoCaM by more than fivefold (Fig 2E; Table 4). Combining the apoCaM E88K mutation with the IQ peptide alteration K1662E restored the binding affinity to some degree although not completely (Fig 2E). The apoCaM mutant F90A showed a ~3.3-fold decrease in binding affinity for WT IQ peptide (Fig 2F; Table 4). Consistently, I1654A and F1658A substitutions in the IQ peptide resulted in a comparable reduction in their affinity for apoCaM (Fig 2F). These results confirmed three important intermolecular interactions that had been seen in the NMR structure: (i) a salt bridge between IQ residue K1662 and apoCaM residue E88; (ii) hydrophobic contact between IQ residue I1654 and apoCaM residue F90; and (iii) hydrophobic contact between IQ residue F1658 and apoCaM residues F90 and M110.

### $\alpha$ -Actinin and apoCaM do not form a ternary complex with Ca<sub>v</sub>1.2 IQ

The structures of  $\alpha$ -actinin-1 (Fig 1) and apoCaM (Fig 2) each bound to the IQ peptide reveal that both binding sites are structurally overlapped and therefore should preclude formation of a ternary complex ( $\alpha$ -actinin-1/IQ/apoCaM), in contrast to what was suggested previously (Hall *et al*, 2013). The possibility of ternary complex formation was further ruled out by NMR titrations (Fig EV3). The NMR spectrum of <sup>15</sup>N-labeled  $\alpha$ -actinin-1 EF-hand domain (Fig EV3A, black peaks) exhibited spectral changes upon the addition of an equivalent amount of unlabeled IQ peptide (Fig EV3A, red peaks marked by arrows) that are reversed by the addition of fivefold excess of unlabeled apoCaM (Fig EV3A, green peaks marked by arrows). This result indicates that  $\alpha$ -actinin-1 and apoCaM both compete for binding to the IQ peptide, which implies that  $\alpha$ -actinin-1 and apoCaM do not simultaneously bind to Ca<sub>v</sub>1.2 IQ and therefore rules out the possibility of a ternary complex. A similar result was observed for the NMR titration with <sup>15</sup>N-labeled apoCaM binding to unlabeled IQ (Fig EV3B). The IQ-induced spectral changes to apoCaM are reversed by the addition of fivefold excess of unlabeled  $\alpha$ -actinin-1 (Fig EV3B, green peaks marked by arrows), demonstrating that  $\alpha$ -actinin-1 and apoCaM do not bind simultaneously to the IQ peptide, which argues against a ternary complex.

### $\alpha$ -Actinin binding to the Ca<sub>v</sub>1.2 IQ motif augments open probability of individual channels

Point mutations that impaired  $\alpha$ -actinin binding to the IQ motif of  $\alpha_1$ 1.2 reduced current density upon reconstitution of Ca<sub>v</sub>1.2 in HEK293 cells by 70–80% but surface expression by only 35–40% as determined by two different methods (Tseng *et al*, 2017). We performed cell-attached recordings (Fig 3A) to precisely determine single-channel parameters of Ca<sub>v</sub>1.2 as before (Davare *et al*, 2001; Patriarchi *et al*, 2016; Qian *et al*, 2017; Bartels *et al*, 2018). All three mutations in the IQ motif that impaired  $\alpha$ -actinin binding (Table 2) (Tseng *et al*, 2017), i.e., K1647A, Y1649A, and I1654A, decreased functional availability by 79–93%, ensemble averages by 84–91%, and single-channel activity by ~85–92% without affecting unitary current amplitudes (i) (Figs 3B–G and EV4).

The single-channel activity is the product of the number (N) of channels in a patch, the open probability (P<sub>o</sub>), and unitary current amplitudes (i) of each individual channel (i.e., N·P<sub>o</sub>·i). Because i

#### Figure 2. ApoCaM forms electrostatic and hydrophobic contacts with Ca<sub>v</sub>1.2.

- Ensemble of 10 lowest energy NMR-derived structures of apoCaM/IQ complex. Structural statistics are given in Table 3.
- Energy-minimized average structure of apoCaM (cyan) bound to IQ (red), showing an intermolecular salt bridge between IQ K1662 and apoCaM E88. The K1662 side-chain amino nitrogen atom is 2.7 Å away from the side-chain carbonyl oxygen of E88.
- Intermolecular hydrophobic contacts between IQ I1654 (red) and apoCaM F90 (cyan). Side-chain atoms colored yellow. The I1654 side-chain methyl carbon atom is 2.2 Å away from the closest aromatic ring atom of F90.
- Intermolecular hydrophobic contacts between F1658 of IQ and F90/M110 in apoCaM. The aromatic side-chain atoms of F1658 are 2.3 and 2.6 Å away from the closest side-chain atom of F90 and M110, respectively.
- FP titrations showing binding of apoCaM to IQ peptides WT (black) and K1662E (red) and of apoCaM mutant E88K to IQ WT (green) and IQ peptide K1662E (blue, “charge inversion”; see Table 4 for binding parameters and standard errors).
- FP titrations showing binding of apoCaM to IQ peptides WT (black), I1654A (red), and F1658A (green) and of apoCaM mutant F90A to IQ WT (blue; see Table 4 for binding parameters and standard errors).

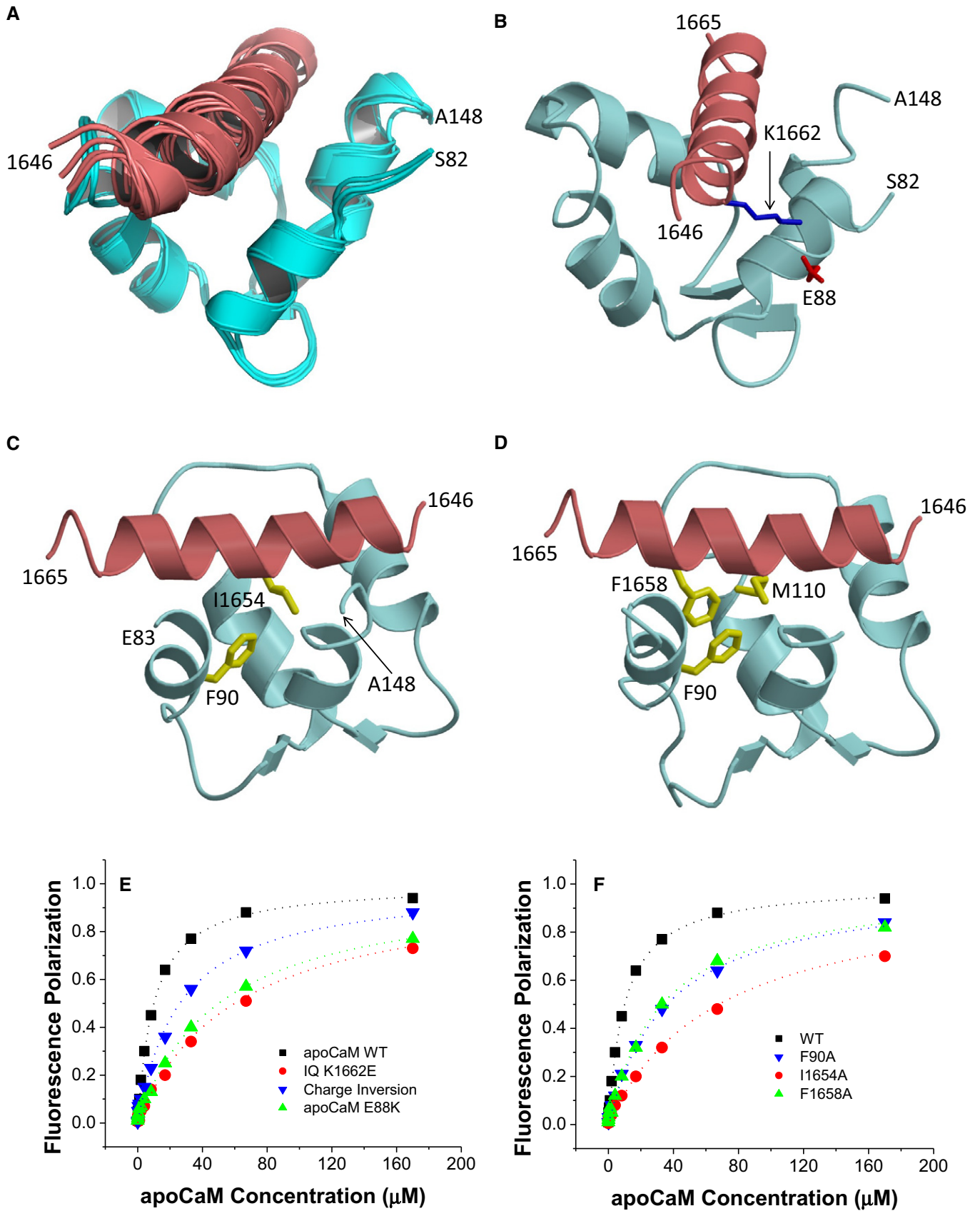


Figure 2.

**Table 3. NMR structural statistics for apoCaM/IQ.**

NMR structural restraints	
Hydrogen bonds	62
RDC Q-Factor	0.089
<sup>1</sup> D <sub>HN</sub> RDC	36
RDC Correlation Coefficient (R)	0.99
Root mean squared deviation from average structure	
CaM backbone atoms	0.6 Å ± 0.3 for 200 structures
CaM backbone atoms (refined)	0.6 Å ± 0.2 for 92 structures
Haddock scoring	
Cluster size	200
Van der Waals energy	-56.8 ± 0.6
Electrostatic energy	-463.5 ± 20.7
Restraints violation energy	99.8 ± 36.2
Ramachandran plot	
Most favored regions	89.8%
Allowed regions	8.0%
Unfavored regions	2.3%

was unaffected (Fig 3F), the mutations must affect NPo. Given that surface expression of all three mutations decreased by only 35–40% versus WT  $\alpha_1$ 1.2 under exactly the same conditions (Tseng *et al*, 2017), the ~90% reduction of NPo for all three mutants to ~10% of WT Ca<sub>v</sub>1.2 suggests that Po of the remaining ~60% channels is only ~1/6 of the Po of WT Ca<sub>v</sub>1.2. These observations suggest a remarkable ~6-fold decrease in Po upon loss of  $\alpha$ -actinin binding. To corroborate this notion, we determined N for each recording and derived Po for individual channels. Accordingly, Po is reduced by ~90% for individual channels carrying a K1647A, Y1649A, or I1654A mutation (Fig 3E; Table 5a–e). At the same time, the F1658A and K1662E mutations, which diminish apoCaM binding, did not alter NPo (Table 5f,g).

To further scrutinize the role of  $\alpha$ -actinin in Po of Ca<sub>v</sub>1.2, Ca<sub>v</sub>1.2 was co-expressed with WT  $\alpha$ -actinin-1 or its binding-deficient E847K/E851K mutant (Fig 4A) and availability, NPo, Po, i, and assemble averages determined (Fig 4B–G). Overexpression of WT

**Table 4.  $K_d$  (in  $\mu$ M; means  $\pm$  SEM) for apoCaM binding to IQ as determined by FP.**

	apoCaM		
	WT	E88K	F90A
Ca <sub>v</sub> 1.2 IQ			
WT	10 ± 3	50 ± 10	33 ± 5
K1647E	12 ± 3	53 ± 1.0	/
K1647A	11 ± 3	/	/
Y1649A	16 ± 4	/	/
I1654A	68 ± 1.0	/	/
F1658A	33 ± 5	/	/
K1662E	60 ± 10	26 ± 5	/

Shown are mean  $\pm$  SD ( $n = 3$  for all conditions).

but not E847K/E851K mutant  $\alpha$ -actinin-1 increased Po of Ca<sub>v</sub>1.2 WT by more than twofold from 3.4% seen with Ca<sub>v</sub>1.2 alone to 7.9% (Fig 4E; Table 6a–c). Availability, NPo, and assemble averages but not unitary current amplitudes were also increased by WT but not E847K/E851K mutant  $\alpha$ -actinin-1 (Fig 4B, C, D, F and G; Table 6a–c). Accordingly, in HEK293 cells functional occupancy of Ca<sub>v</sub>1.2 by endogenous  $\alpha$ -actinin appears to be far from complete.

To further test whether  $\alpha$ -actinin needs to bind to the Ca<sub>v</sub>1.2 IQ motif to augment Po, we used a charge inversion experiment by mutating K1647 to the negatively charged glutamyl rather than neutral alanyl residue and then attempted rescue of the expected reduction in Po by pairing expression of K1647E Ca<sub>v</sub>1.2 with charge-inverted E847K/E851K  $\alpha$ -actinin-1. Co-expression of K1647E mutant Ca<sub>v</sub>1.2 with WT  $\alpha$ -actinin-1 yielded a low availability, NPo, Po, and ensemble average (Fig 5C–E and G; Table 6d), which were well below the values observed upon expression of WT Ca<sub>v</sub>1.2 alone or co-expression of WT Ca<sub>v</sub>1.2 with E847K/E851K mutant  $\alpha$ -actinin-1 (Fig 4C–E and G; Table 6a–c). The reduction in availability was statistically significantly, though not fully, rescued when K1647E mutant Ca<sub>v</sub>1.2 was paired with E847K/E851K mutant rather than WT  $\alpha$ -actinin-1 (Fig 5A; Table 6e). Po also appears to be partially rescued although the  $P$  value was 0.07 versus pairing of WT  $\alpha$ -actinin-1 with K1647E mutant Ca<sub>v</sub>1.2. This rescue of loss of availability and likely Po for K1647E mutant Ca<sub>v</sub>1.2 by E847K/E851K mutant  $\alpha$ -actinin-1 must be due to either enhanced opening of individual channels, a change in channel surface expression, or both. This rescue is difficult to explain by a mechanism other than that  $\alpha$ -actinin-1 binding augments channel activity, including binding of endogenous apoCaM. Consistently, impairing apoCaM binding to the Ca<sub>v</sub>1.2 IQ motif by mutating F1658 to Ala or K1662 to Glu had no effect on availability, NPo, and Po, and did not affect ensemble averages (Fig 3C–G; Table 5).

One possibility for a reduction in Po is that K1647A, Y1649A, and I1654A shift the voltage dependence of Ca<sub>v</sub>1.2 to more positive potentials such that WT channels open upon depolarization to 0 mV more readily than mutant channels. However, neither the reversal potential nor the voltage dependence of activation was significantly affected by the K1647A and Y1649A mutations and only minimally by the I1654A mutation (Appendix Fig S3; Table 7a–d).

To test whether this charge inversion rescue for the K1647E mutant promoted surface expression of Ca<sub>v</sub>1.2, we performed surface biotinylation experiments (Fig 6). As expected, co-expression of WT  $\alpha$ -actinin-1 with WT Ca<sub>v</sub>1.2 increased  $\alpha_1$ 1.2 biotinylation by ~60% versus WT  $\alpha_1$ 1.2 alone. Thus, WT Ca<sub>v</sub>1.2 expression at the surface is enhanced by  $\alpha$ -actinin-1 (Fig 6A). That the increase in surface expression of WT Ca<sub>v</sub>1.2 by WT  $\alpha$ -actinin-1 overexpression was smaller than the increase in Po is analogous to the smaller effects of the  $\alpha_1$ 1.2 K1647A, Y1649A, and I1654A mutations on surface expression compared to charge density (Tseng *et al*, 2017) and the larger decrease in Po and NPo we report here (Fig 3). Importantly, this increase in Ca<sub>v</sub>1.2 surface expression by  $\alpha$ -actinin-1 was not seen when WT  $\alpha_1$ 1.2 was co-expressed with E847K/E851K mutant  $\alpha$ -actinin-1 or K1647E mutant  $\alpha_1$ 1.2 with WT  $\alpha$ -actinin-1 (Fig 6B). However, the charge inversion we performed by combining these mutants failed to increase surface expression of Ca<sub>v</sub>1.2 to a degree that would be detectable (Fig 6B). This result is in contrast to our findings that K1647E  $\alpha_1$ 1.2 availability and likely Po were partially rescued by the E847K/E851K  $\alpha$ -actinin-1 charge



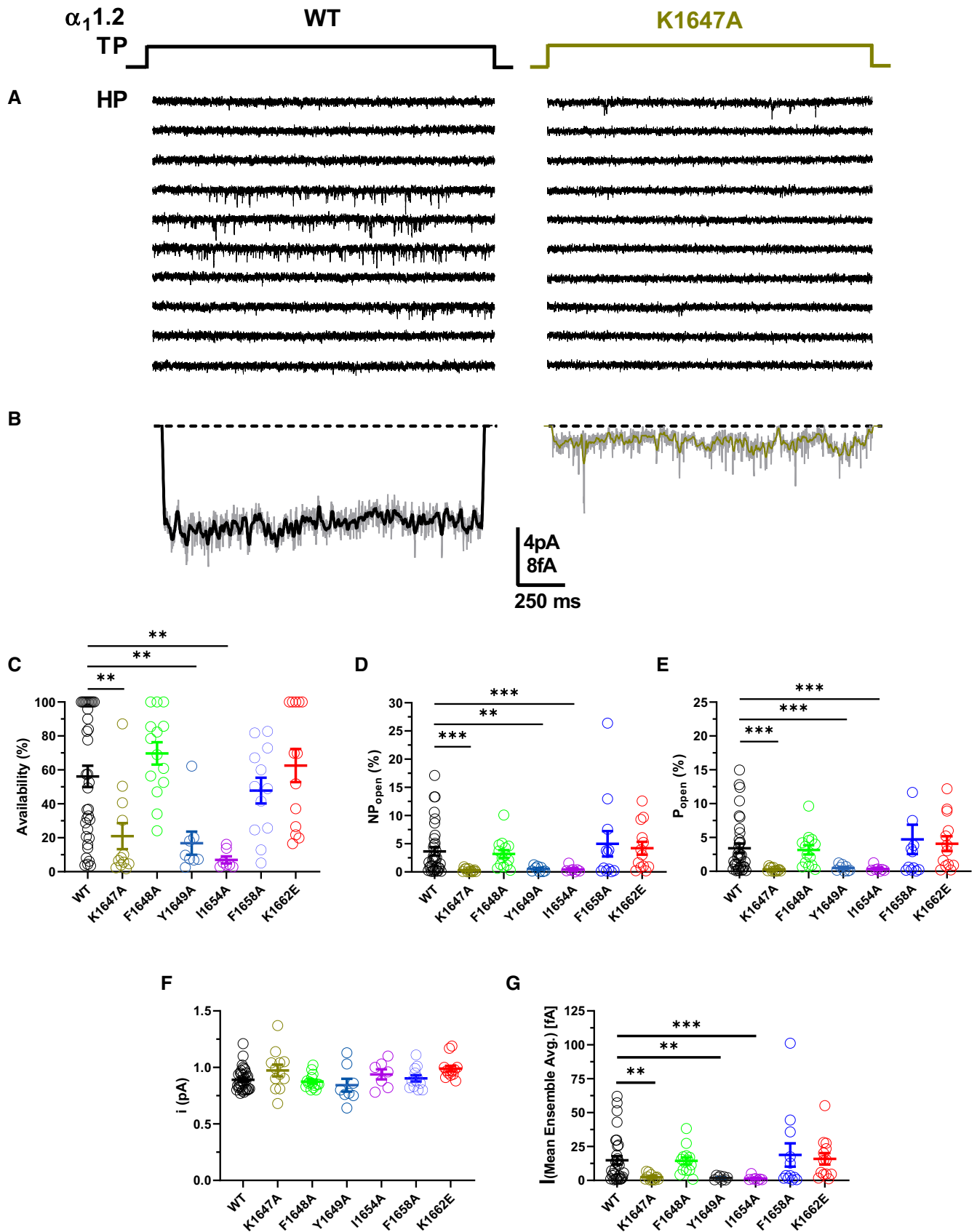


Figure 3.

**Figure 3. Ca<sub>v</sub>1.2 mutations that affect  $\alpha$ -actinin-1 drastically decrease channel open probability.**

HEK293 cells were transfected with  $\alpha_1$ 1.2,  $\alpha_2\delta$ -1, and  $\beta_{2A}$  and cultured for 22–24 h before cell-attached patch recording in 110 mM Ba<sup>2+</sup>.

- A Single Ca<sub>v</sub>1.2 channel recordings of Ca<sub>v</sub>1.2 WT and K1647A. Holding potential (HP) was –80 mV and test potential (TP) 0 mV. Shown are 10 consecutive sweeps from representative experiments (see Fig EV4 for more sweeps).
- B Mean assemble averages for all experiments with Ca<sub>v</sub>1.2 WT and K1647A, which are based on a total of 2,744 and 868 sweeps, respectively (see Table 5).
- C–G Dot plots and means  $\pm$  SEM for availability (i.e., likelihood that a sweep had at least one event; C), NPo (D), Po (E), unitary current amplitude i (F), and the mean of the current of a single channel at any point in time calculated from the ensemble averages of each experiment (G) (\*\**P* < 0.01, \*\*\**P* < 0.001 compared to WT; one-way ANOVA with Bonferroni post hoc test (C) or Welch ANOVA with Tamhane T2 test (D–G); *n* = 7–35. see Table 5 for more details).

**Table 5. Biophysical properties of Ca<sub>v</sub>1.2 microscopic single-channel currents for WT versus IQ motif mutants.**

Gating parameter	Availability (%)	NP <sub>open</sub> (%)	P <sub>open</sub> (%)	I (mean ensemble avg.) [fA]	Unitary current (pA)	Sweeps	<i>n</i>
WT (a)	56.2 $\pm$ 6.3	3.6 $\pm$ 0.75	3.4 $\pm$ 0.7	14.8 $\pm$ 3.1	0.89 $\pm$ 0.02	2,744	32–35
K1647A (b)	21.0 $\pm$ 7.6**	0.30 $\pm$ 0.09***	0.27 $\pm$ 0.08***	2.3 $\pm$ 0.6**	0.97 $\pm$ 0.05	868	12
F1648A (c)	69.7 $\pm$ 6.6	3.2 $\pm$ 0.7	3.2 $\pm$ 0.7	14.4 $\pm$ 2.6	0.87 $\pm$ 0.02	1,221	13–14
Y1649A (d)	16.8 $\pm$ 6.8**	0.53 $\pm$ 0.17**	0.49 $\pm$ 0.2***	1.9 $\pm$ 0.5**	0.84 $\pm$ 0.06	556	8
I1654A (e)	7.0 $\pm$ 2.1**	0.44 $\pm$ 0.2***	0.35 $\pm$ 0.2***	1.4 $\pm$ 0.6***	0.94 $\pm$ 0.04	589	7
F1658A (f)	47.8 $\pm$ 7.6	5.0 $\pm$ 2.2	4.7 $\pm$ 2.2	18.8 $\pm$ 8.6	0.90 $\pm$ 0.03	986	12
K1662E (g)	62.5 $\pm$ 9.7	4.2 $\pm$ 1.1	4.1 $\pm$ 1.1	15.9 $\pm$ 4.2	0.99 $\pm$ 0.03	1,015	13
One-Way ANOVA	a-b <sup>†</sup>	a-b <sup>‡</sup>	a-b <sup>‡</sup>	a-b <sup>‡</sup>	NS		
	a-d <sup>†</sup>	a-d <sup>‡</sup>	a-d <sup>‡</sup>	a-d <sup>‡</sup>			
	a-e <sup>†</sup>	a-e <sup>‡</sup>	a-e <sup>‡</sup>	a-e <sup>‡</sup>			

HEK293 cells were transiently transfected with WT and IQ domain mutant Ca<sub>v</sub>1.2 ( $\alpha_1$ 1.2,  $\alpha_2\delta$ -1, and  $\beta_{2A}$ ) for recording of single-channel activity in 110 mM Ba<sup>2+</sup> upon depolarized from a holding potential –80 mV to a test potential (TP) of 0 mV for 2 s at an interpulse rate of 0.14 Hz. Availability is quantified as the fraction of sweeps showing channel activity over the number of total sweeps. Statistical significance was determined by pairwise multiple testing WT (a) against K1647A (b), F1648A (c), Y1649A (d), I1654A (e), F1658A (f), and K1662E (g) by a one-way ANOVA with Bonferroni<sup>†</sup> post hoc test or Welch ANOVA with Tamhane<sup>‡</sup> T2 test. Given are mean values  $\pm$  SEM (\**P* < 0.05, \*\**P* < 0.01, \*\*\**P* < 0.0001).

reversal (Fig 5). It is conceivable that a small rescue effect did occur but was indiscernible for statistical reasons as 95% confidence intervals (CIs) are larger than a potentially partial rescue of, e.g., 30% of the impairment of ~50% by the K1647E mismatch with WT  $\alpha$ -actinin-1 (Appendix Table S1; a 30% rescue would translate into only an ~15% increase in surface expression).

 **$\alpha$ -Actinin binding to the Ca<sub>v</sub>1.2 IQ motif augments gating charge movement as well as its coupling to channel opening**

To test the molecular mechanism underlying the  $\alpha$ -actinin-induced increase in Po in more detail, we analyzed gating charge movement at the Ba<sup>2+</sup> current reversal potential (Fig 7) by whole-cell patch-clamp recording. This approach measures all of the Ca<sup>2+</sup> channels on the surface, thereby ruling out any potential limitation caused by the channel selection inherent in the cell-attached patch recordings in Figs 3–5. The K1647A, Y1649A, and I1654A mutations reduced gating currents (Q<sub>on</sub>) by 66–77% (Fig 7A, B and D; Table 7) suggesting that  $\alpha$ -actinin fosters gating charge movement. This reduction is stronger than the reduction in surface expression (Tseng *et al*, 2017) but not quite as strong as the 90% reduction in NPo for these mutants (Fig 5). Thus, we investigated whether  $\alpha$ -actinin also augments coupling of gating charge movement to channel opening. We analyzed the relationship of tail currents (I<sub>tail</sub>) to Q<sub>on</sub> and determined the slopes of the regression curves as an established parameter for quantification of the coupling of Q<sub>on</sub> to I<sub>tail</sub> (Tuluc *et al*, 2009; Yang *et al*, 2010). Accordingly, the slopes for

K1647A, Y1649A, and I1654A mutant Ca<sub>v</sub>1.2 were strongly reduced compared to WT (Fig 7C; Table 7a–d). Because large gating events were rare for these mutants, we combined all data from those three mutants for further analysis to better cover that range of the curve. This analysis confirmed that the slope of the resulting curve was substantially smaller than for WT Ca<sub>v</sub>1.2 (Fig 7E). Collectively, these data indicate that binding of  $\alpha$ -actinin to the Ca<sub>v</sub>1.2 IQ motif augments not only surface expression but also gating charge movement and its coupling to channel opening. Neither gating charge movements nor their coupling to channel opening were significantly affected by the F1658A or K1662E mutations (Fig 7; Table 7e,f), once more arguing against a role in apoCaM binding to the IQ motif in defining NPo under basal conditions.

**Discussion**

The NMR structures of  $\alpha$ -actinin-1 and apoCaM bound to the Ca<sub>v</sub>1.2 IQ motif presented here revealed distinct intermolecular interactions that were verified by mutagenesis experiments involving charge inversion for both interactions. The EF hands in  $\alpha$ -actinin-1 are not capable of binding to Ca<sup>2+</sup> under physiological conditions because their EF-hand loops lack the proper residues for ligating Ca<sup>2+</sup> with high affinity (Backman, 2015). Therefore, the  $\alpha$ -actinin-1 EF-hand domain bound to Ca<sub>v</sub>1.2 is in the Ca<sup>2+</sup>-free state under basal conditions ([Ca<sup>2+</sup>]<sub>i</sub> of ~100 nM) and adopts a semi-open conformation of Ca<sup>2+</sup>-free EF hands like that

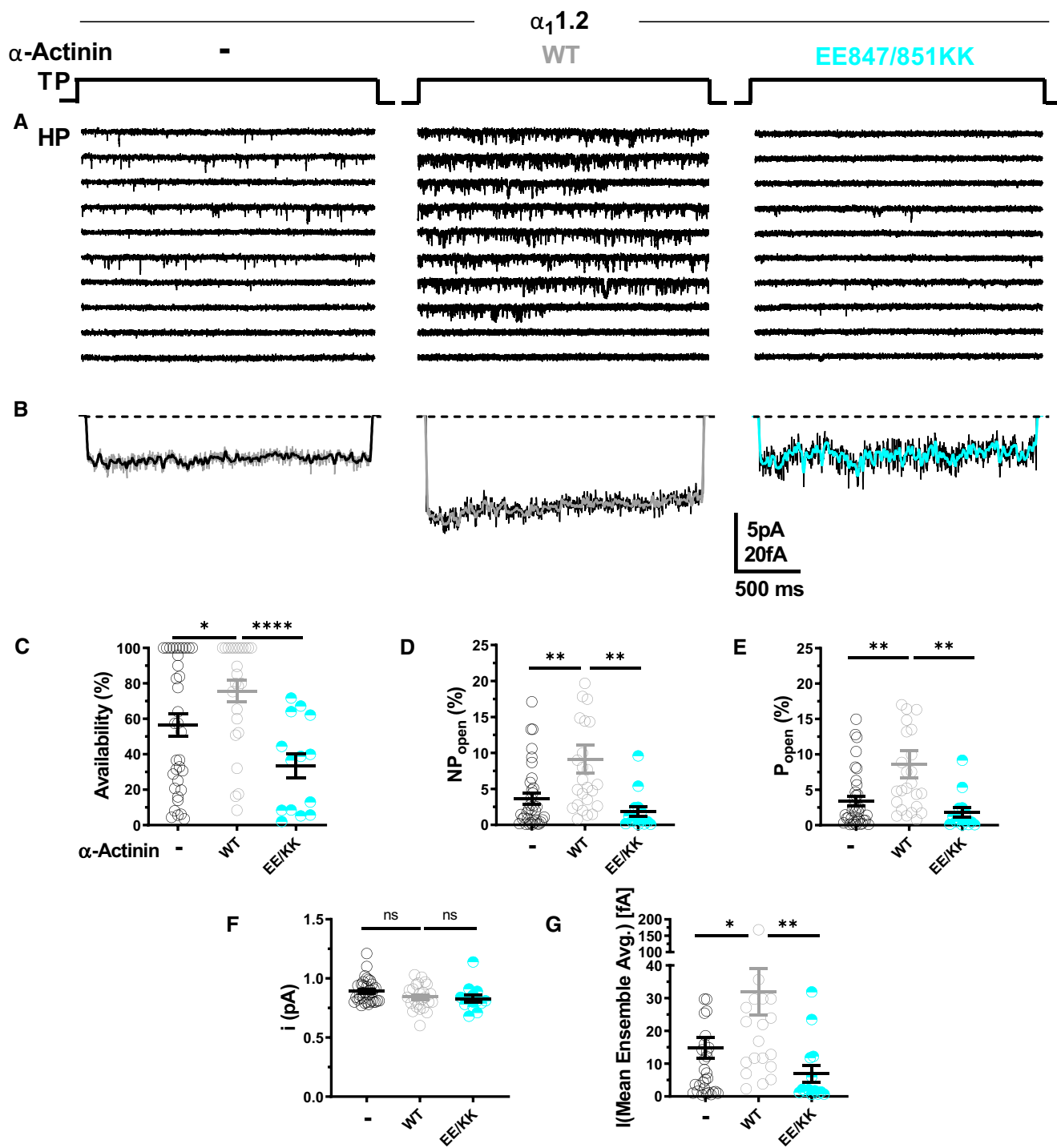


**Figure 4. Ectopic  $\alpha$ -actinin-1 expression increases  $\text{Ca}_v1.2$  open probability.**

HEK293 cells were transfected with  $\alpha_11.2$ ,  $\alpha_2\delta-1$ , and  $\beta_{2A}$  plus, if indicated,  $\alpha$ -actinin-1 before cell-attached patch recording.

A Representative single  $\text{Ca}_v1.2$  channel recordings of WT  $\text{Ca}_v1.2$  alone or with WT or E847K/E851K mutant  $\alpha$ -actinin-1.

B Mean ensemble averages for all experiments for each combination.

C-G Dot plots and means  $\pm$  SEM for availability (C), NPo (D), Po (E), unitary current amplitude  $i$  (F), and the mean of the current of a single channel calculated from the ensemble averages of each experiment (G) (\* $P < 0.05$ , \*\* $P < 0.01$ , \*\*\*\* $P < 0.001$ ; unpaired t-test;  $n = 13-35$ ; see Table 6 for more details).

**Table 6. Effect of  $\alpha$ -actinin-1 ectopic expression on biophysical properties of Ca<sub>v</sub>1.2 single-channel currents.**

Gating parameter	Availability (%)	NP <sub>open</sub> (%)	P <sub>open</sub> (%)	I (Mean ensemble Avg.) [fA]	Unitary current (pA)	Sweeps	n
WT (a)	56.6 ± 6.3	3.6 ± 0.75	3.4 ± 0.69	14.8 ± 3.1	0.89 ± 0.02	2,744	32–35
WT + $\alpha$ -Actinin (b)	76.5 ± 6.2*	9.2 ± 2.0**	7.9 ± 2.0*	31.3 ± 7.5*	0.84 ± 0.02	2,388	23–25
WT + EE847/851KK (c)	32.9 ± 7.5****	1.9 ± 0.7**	1.8 ± 0.7*	7.4 ± 2.8*	0.83 ± 0.03	1,252	13
K1647E + $\alpha$ -Actinin (d)	43 ± 5.0	1.8 ± 0.3	1.7 ± 0.3	8.5 ± 1.5	0.83 ± 0.01	2,601	30
K1647E + EE847/851KK (e)	67.9 ± 6.9**	2.6 ± 0.5	2.5 ± 0.5	11.3 ± 2.7	0.84 ± 0.02	1,376	16
Unpaired t-test	a-b <sup>‡</sup>	a-b <sup>‡</sup>	a-b <sup>‡</sup>	a-b <sup>‡</sup>	NS		
	b-c <sup>‡</sup>	b-c <sup>‡</sup>	b-c <sup>‡</sup>	b-c <sup>‡</sup>			
	d-e <sup>‡</sup>		d-e P = 0.7	d-e P = 0.7			

HEK293 cells were transiently transfected with WT Ca<sub>v</sub>1.2 ( $\alpha_1$ 1.2,  $\alpha_2$ . $\delta_1$ , and  $\beta_{2a}$ ) and, if indicated, with  $\alpha$ -actinin-1 WT or E847K/E851K. Single-channel activity was obtained as in Table 5. Statistical significance was determined by pairwise testing of Ca<sub>v</sub>1.2 WT alone (a) versus Ca<sub>v</sub>1.2 WT +  $\alpha$ -actinin WT (b), Ca<sub>v</sub>1.2 WT +  $\alpha$ -actinin-1 WT versus Ca<sub>v</sub>1.2 +  $\alpha$ -actinin-1 E847K/E851K (c), and Ca<sub>v</sub>1.2 K1647E +  $\alpha$ -actinin-1 WT (d) versus Ca<sub>v</sub>1.2 K1647E +  $\alpha$ -actinin-1 E847K/E851K (e) with an unpaired t-test<sup>‡</sup>. Given are mean values ± SEM (\*P < 0.05, \*\*P < 0.01, \*\*\*\*P < 0.0001). Values for Ca<sub>v</sub>1.2 WT are provided for comparison from Table 5.

observed for apoCaM bound to various target proteins (Houdusse *et al*, 2006; Chagot & Chazin, 2011; Feldkamp *et al*, 2011). However, the semi-open EF-hand conformation of  $\alpha$ -actinin-1 binds to the IQ peptide with a polarity opposite to that of apoCaM (see black arrows in Fig EV5A and B). The Ca<sub>v</sub>1.2 residue K1647 at the N-terminal end of the IQ helix forms intermolecular salt bridges with  $\alpha$ -actinin-1 residues E847 and E851. By stark contrast, the IQ helix is rotated 180 degrees upon binding to apoCaM (see black arrows in Fig EV5). This opposite orientation places Ca<sub>v</sub>1.2 residue K1662 at the C-terminal end of the IQ helix in close proximity to CaM residues E85 and E88, which are homologous to  $\alpha$ -actinin-1 residues E847 and E851. Similarly, the IQ helices in voltage-gated Na<sup>+</sup> channels bind to apoCaM and Ca<sup>2+</sup>-saturated CaM with opposite polarity (Hovey *et al*, 2017). Thus, the orientation of the IQ helix bound to the EF-hand motif may be an important structural determinant of binding specificity and may explain why  $\alpha$ -actinin-1 and apoCaM have different functional effects.

Voltage-gated Na<sup>+</sup> channels exhibit Ca<sup>2+</sup>-dependent inactivation (CDI) mediated by Ca<sup>2+</sup>-CaM (Ben-Johny *et al*, 2014; Gabelli *et al*, 2016), similar to Ca<sub>v</sub>1.2 (Peterson *et al*, 1999; Zuhlke *et al*, 1999). However, the structure of apoCaM bound to the Ca<sub>v</sub>1.2 IQ motif (Fig EV5B) is quite different from previous structures of apoCaM bound to Na<sub>v</sub>1.2 (Fig EV5C) or Na<sub>v</sub>1.5 (Chagot & Chazin, 2011; Gabelli *et al*, 2014). The Na<sub>v</sub>1.2 IQ motif sequence is only 17% identical to that of Ca<sub>v</sub>1.2 (Fig EV5D). Na<sub>v</sub>1.2 residues A1909, A1915, and Y1919, which are not conserved in Ca<sub>v</sub>1.2, each make critical contacts with apoCaM (Fig EV5C). The side-chain methyl groups of A1909 and A1915 are each 2.5 Å away from the side-chain methyl atoms of CaM residues M109 and L85, respectively. The aromatic side chain of Y1919 is in intimate contact with the aromatic side chain of F141 from CaM. Another important difference is that the Ca<sub>v</sub>1.2 IQ helix binds to apoCaM with opposite directionality compared to the Na<sub>v</sub>1.2 IQ helix (see black arrows in Fig EV5B and C). Hence, the salt bridge that connects Ca<sub>v</sub>1.2 (K1662) to apoCaM (E88) is not conserved in Na<sub>v</sub>1.2 or Na<sub>v</sub>1.5 but the large number of non-conserved intermolecular hydrophobic contacts to Na<sub>v</sub>1.2 (Fig EV5C) caused by the opposite binding orientation of the IQ helix should outweigh any stabilization from the salt bridge in Ca<sub>v</sub>1.2 and may explain why apoCaM binds to Na<sub>v</sub>1.2 and Na<sub>v</sub>1.5

with nanomolar affinity (Hovey *et al*, 2017) compared to the much weaker micromolar affinity of apoCaM binding to Ca<sub>v</sub>1.2 (Table 4).

The relatively high dissociation constant for apoCaM binding to the  $\alpha_1$ 1.2 IQ motif ( $K_d = 10 \mu\text{M}$ ) may be outside the physiological concentration range for apoCaM in neurons. Under basal conditions, the cytosolic apoCaM is kept below 1  $\mu\text{M}$  (Wu & Bers, 2007) by proteins that have a high affinity for apoCaM. For instance, in neurons neurogranin (RC3) (Huang *et al*, 2000, 2004; Ran *et al*, 2003; Zhong *et al*, 2011) and GAP-43 (P-57) (Cimler *et al*, 1985) serve as sinks and reservoirs for apoCaM. In neurons, total concentration of CaM is ~10  $\mu\text{M}$  (Egrie *et al*, 1977; Zhabotinsky *et al*, 2006), of neurogranin is 20  $\mu\text{M}$  (Huang *et al*, 2004; Zhabotinsky *et al*, 2006), and of GAP-43 is 18  $\mu\text{M}$  (Cimler *et al*, 1985; Zhabotinsky *et al*, 2006), and their  $K_d$  values for apoCaM are in the range of 1–5  $\mu\text{M}$  (Alexander *et al*, 1987; Huang *et al*, 2000; Zhabotinsky *et al*, 2006), resulting in 0.9  $\mu\text{M}$  free CaM under basal conditions (Zhabotinsky *et al*, 2006). Therefore, on the basis of the relatively low binding affinity of apoCaM ( $K_d = 10 \mu\text{M}$ ), the fractional binding of apoCaM to  $\alpha_1$ 1.2 can be estimated to be < 10% ( $Y = \frac{[CaM]}{[CaM] + K_d} < 0.1$ ) under basal physiological conditions in neurons. Recent work suggests that ectopically expressed WT CaM as well as Ca<sup>2+</sup> binding-deficient CaM<sub>1234</sub> is in large excess over endogenous CaM (Iacobucci & Popescu, 2017). As a result, CaM<sub>1234</sub> may occupy a much larger fraction of  $\alpha_1$ 1.2 than the endogenous WT apoCaM. In this scenario, expression of CaM<sub>1234</sub> could impair CDI as seen earlier (Peterson *et al*, 1999) by mechanisms other than displacement of endogenous apoCaM as invoked earlier (Peterson *et al*, 1999).

Alterations of I1609 in  $\alpha_1$ 1.3 (equivalent to I1654 in  $\alpha_1$ 1.2) impair binding of apoCaM to the closely related Ca<sub>v</sub>1.3 channel and Po, which was interpreted to mean that apoCaM binding to this IQ motif augments Po (Adams *et al*, 2014). Here, we show that the homologous I1654 in the highly conserved IQ motif of Ca<sub>v</sub>1.2 is not only critical for apoCaM but also  $\alpha$ -actinin binding. Accordingly, mutating I1609 could have decreased NPo by impairing  $\alpha$ -actinin rather than apoCaM binding. Indeed, cell-attached channel recordings showed an ~90% reduction in Po for all three  $\alpha$ -actinin binding-deficient  $\alpha_1$ 1.2 IQ mutants. This effect included K1647, which contacts  $\alpha$ -actinin (Fig 1C) but not apoCaM. Consistently, the K1647A mutation reduced binding of  $\alpha$ -actinin (Table 2) but not apoCaM

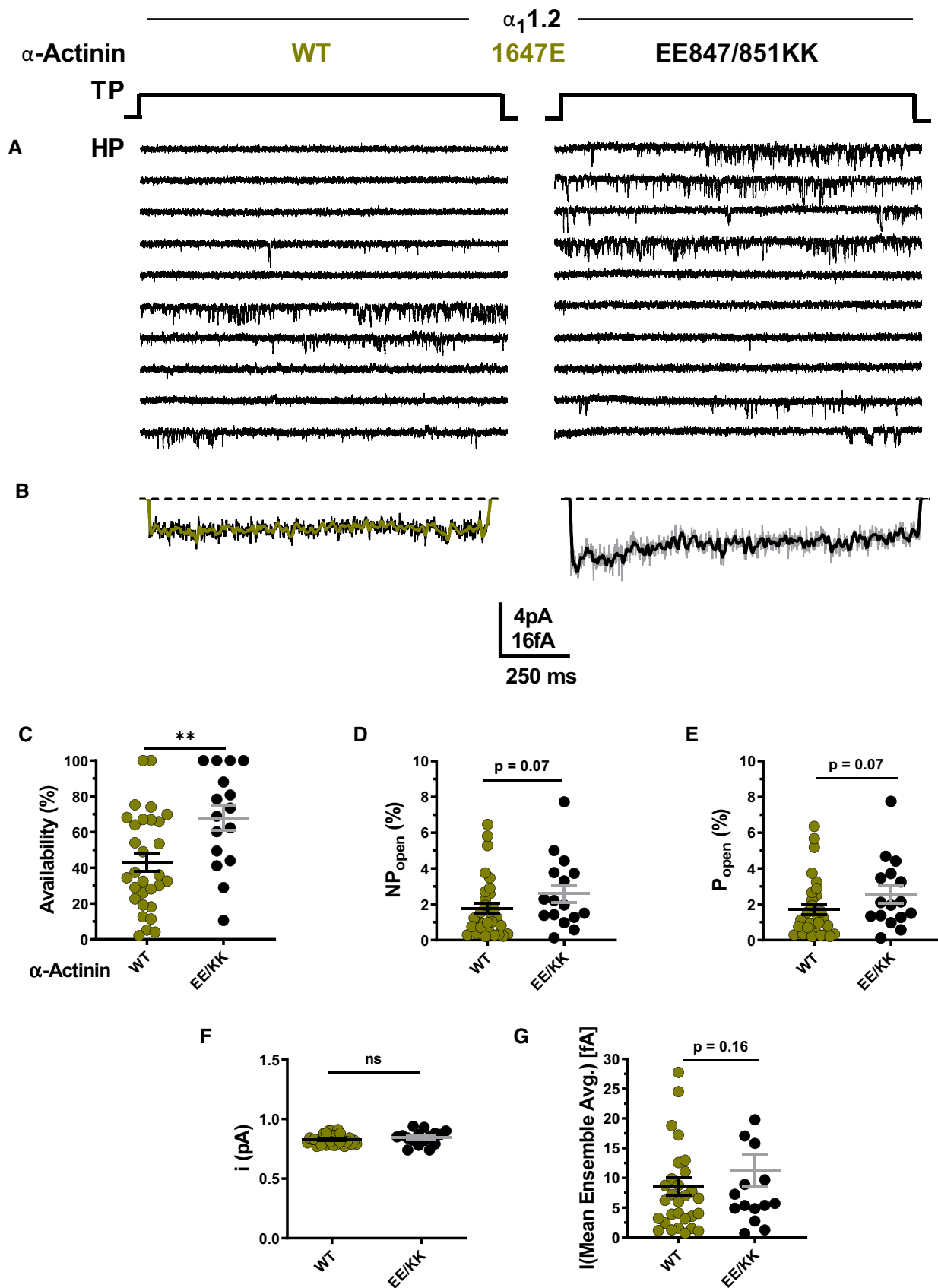


Figure 5.



**Figure 5.  $\alpha$ -Actinin-1 E847K/E851K partially rescues open probability for  $\text{Ca}_v1.2$  K1647E.**

HEK293 cells were transfected with  $\alpha_1.2$  with the K1647E mutation,  $\alpha_2\delta-1$ , and  $\beta_{2A}$  plus  $\alpha$ -actinin-1 WT or E847K/E851K before cell-attached patch recording.

A Representative single  $\text{Ca}_v1.2$  channel recordings of  $\text{Ca}_v1.2$  K1647E with WT or E847K/E851K  $\alpha$ -actinin-1.

B Mean assemble averages for all experiments for both combinations.

C–G Dot plots and means  $\pm$  SEM for availability (C), NPo (D), Po (E), unitary current amplitude  $i$  (F), and mean of the current of a single channel calculated from the ensemble averages of each experiment (G) (\*\* $P < 0.01$ ; unpaired  $t$ -test;  $n = 16$ –30; see Table 6 for more details).

(Table 4). The same is true for the Y1649A mutation. Although Y1649 does not form a direct interaction with  $\alpha$ -actinin EF3-EF4, the Y1649A mutation does abrogate  $\alpha$ -actinin binding in the yeast two-hybrid system (Tseng *et al*, 2017). We suggest that Y1649 is necessary to stabilize the orientation of L1653 and neighboring I1654, which is required for binding to  $\alpha$ -actinin (Appendix Fig S4A). Thus, our new data indicate that Po is largely determined by  $\alpha$ -actinin and not apoCaM binding. In fact, the F1658A and K1662E mutations, which decreased apoCaM binding (Table 4), did affect neither Po (Fig 3E) nor  $Q_{on}$  (Fig 7A, B and D) and minimally if at all  $\alpha$ -actinin binding (Table 2). In support of these results, others found no effect of CaM on  $\text{Ca}_v1.2$  plasma membrane targeting in HEK293 cells (Bourdin *et al*, 2010). This conclusion is further supported by the charge inversion experiments of K1647E mutant  $\alpha_1.2$  and E847K/E851K mutant  $\alpha$ -actinin-1 in which impaired functional channel availability and likely impaired Po are partially rescued (Fig 5). These findings support the functional relevance of the interaction of the positively charged K1647 in the IQ motif with the negatively charged E847 and E851 of  $\alpha$ -actinin-1. That the rescue of the reduction in Po of K1647E mutant  $\alpha_1.2$  by E847K/E851K mutant  $\alpha$ -actinin-1 is far from complete can in part be explained by analysis of the E851K rotamers (Appendix Fig S4B–D). Most of the E851K rotamers are predicted to clash with side-chain and backbone atoms within the  $\alpha$ -actinin region at the channel– $\alpha$ -actinin interface based on our structure (Fig 1C), which will most likely affect the positioning of the EF-hand region of  $\alpha$ -actinin relative to  $\alpha_1.2$  and thereby

the  $\alpha$ -actinin– $\alpha_1.2$  interaction. As a result, binding of E847K/E851K mutant  $\alpha$ -actinin-1 to  $\alpha_1.2$  will be decreased as compared to WT  $\alpha$ -actinin. In fact, binding affinity is also not fully rescued when the K1647E IQ peptide is titrated with E847K/E851K mutant  $\alpha$ -actinin-1 EF3/4 segment (Table 2). A change in the exact structure of the region surrounding the IQ motif in full-length  $\alpha_1.2$  could be the reason for further impairment of  $\alpha$ -actinin binding furnishing a potential explanation for our finding that functional availability and Po are less effectively rescued by the full charge inversion than the *in vitro* binding affinity.

Further mechanistic insight is provided by the strong reduction in gating charge movement upon loss of  $\alpha$ -actinin binding (Fig 7). The most striking and very clear finding for  $Q_{on}$  is the observation that gating charges for the three  $\alpha$ -actinin binding-deficient  $\alpha_1.2$  mutants are so small that they are often barely if at all detectable and amplitudes are difficult to determine. Accordingly,  $\alpha$ -actinin binding to the IQ motif promotes the outward movement of the S4 segments, which gives rise to the gating charges, presumably by either lowering energy barriers for this motion or by stabilizing the “outward” conformation of S4 segments. In addition,  $\alpha$ -actinin binding to the IQ motif augments also the coupling between this gating movement and channel opening. This finding is reminiscent of the effect of  $\text{Ca}_v1.2$  phosphorylation by PKA on S1700, which upregulates this coupling (Fuller *et al*, 2010, 2014). Because of the close proximity of S1700 to the IQ motif, it is tempting to speculate that phosphorylation of S1700 and  $\alpha$ -actinin binding to the IQ motif

**Table 7. Biophysical properties of  $\text{Ca}_v1.2$  macroscopic whole-cell patch currents for WT versus IQ motif mutants.**

Analysis Parameter	I-V			G-V			Charge movement $Q_{on}$ (fC/pF)	$I_{tail}/Q_{on}$ Slope
	$V_{1/2act}$ (mV)	$k_{act}$	$E_{rev}$ (mV)	$V_{1/2act}$ (mV)	$k_{low}$	$k_{high}$		
WT (a)	$-18.5 \pm 0.5$	$-4.2 \pm 0.4$ (10)	$51.3 \pm 1.3$	$-6.5.0 \pm 0.4$	$7.0 \pm 0.3$ (16)	$-8.5 \pm 27.4$	$3.8 \pm 0.9$ (18)	$3.9 \pm 1.5$ (16)
K1647A (b)	$-19.9 \pm 0.9$	$-5.9 \pm 0.6$ (11)	$55.2 \pm 2.0$	$-8.5.0 \pm 0.9$	$8.5 \pm 0.8$ (15)	$9.0 \pm 10.5$	$1.3 \pm 0.3^*$ (15)	$0.26 \pm 1.5$ (15)
Y1649A (c)	$-19.9 \pm 0.6$	$-4.0 \pm 0.5$ (10)	$49.2 \pm 1.5$	$-6.3.0 \pm 0.7$	$7.5 \pm 0.8$ (16)	$28.7 \pm 6.9$	$0.98 \pm 0.3^{**}$ (13)	$0.19 \pm 1.0$ (12)
I1654A (d)	$-12.6 \pm 1.0^{****}$	$-5.4 \pm 0.7$ (5)	$48.2 \pm 2.6$	$-2.5 \pm 0.9^{**}$	$7.5 \pm 0.9$ (13)	$38.5 \pm 11.5$	$0.87 \pm 0.3^{**}$ (13)	$1.3 \pm 0.6$ (12)
F1658A (e)	$-26.5 \pm 1.1^{**}$	$-4.5 \pm 0.9$ (6)	$58.6 \pm 4.1$	$-10.6 \pm 1.4^{**}$	$5.3 \pm 1.6$ (11)	$20.2 \pm 3.9$	$2.8 \pm 0.6$ (13)	$3.1 \pm 1.4$ (12)
K1662E (f)	$-20.2 \pm 0.4$	$-4.2 \pm 0.3$ (12)	$50.1 \pm 1.2$	$-6.1.0 \pm 0.7$	$7.9 \pm 0.8$ (21)	$49.2 \pm 19.4$	$3.5 \pm 1.1$ (17)	$2.2 \pm 1.0$ (14)
ANOVA/ $t$ -test	a-d <sup>†</sup>			a-d <sup>†</sup>			a-b <sup>†</sup>	
							a-c <sup>†</sup>	
	a-e <sup>†</sup>	NS	NS	a-e <sup>†</sup>	NS	NS	a-d <sup>†</sup>	

HEK293 cells were transiently transfected with WT  $\text{Ca}_v1.2$  ( $\alpha_1.2$ ,  $\alpha_2\delta-1$ , and  $\beta_{2A}$ ). Whole-cell patch recording was performed in 20 mM  $\text{Ba}^{2+}$  (see Fig 7). To obtain current–voltage relationships (I-V), currents were recorded upon depolarization from a holding potential of  $-80$  mV to increasingly more positive potentials (see Fig 7A for details). The voltage for half maximal activation ( $V_{1/2act}$ ), activation constant ( $k_{act}$ ), and reversal potential ( $E_{rev}$ ) was determined. To obtain conductance–voltage relationships (G-V), tail currents ( $I_{tail}$ ) were recorded upon repolarization to  $-50$  mV following depolarization from a holding potential of  $-80$  mV to increasingly more positive potentials (see Fig 7A for details). The activation kinetics for G-V were best described by double exponential fits, and the rate constants  $k_{high}$  and  $k_{low}$  were determined accordingly. Total charge movement ( $Q_{on}$ ) and the ratio of  $I_{tail}/Q_{on}$  were determined as in Fig 7. Statistical significance was determined by pairwise multiple testing WT (a) against K1647A (b), Y1649A (c), I1654A (d), F1658A (e), and K1662E (f) by a one-way ANOVA with a Bonferroni<sup>†</sup> post hoc test. Given are mean values  $\pm$  SEM (\* $P < 0.05$ , \*\* $P < 0.01$ , \*\*\*\* $P < 0.0001$ ).

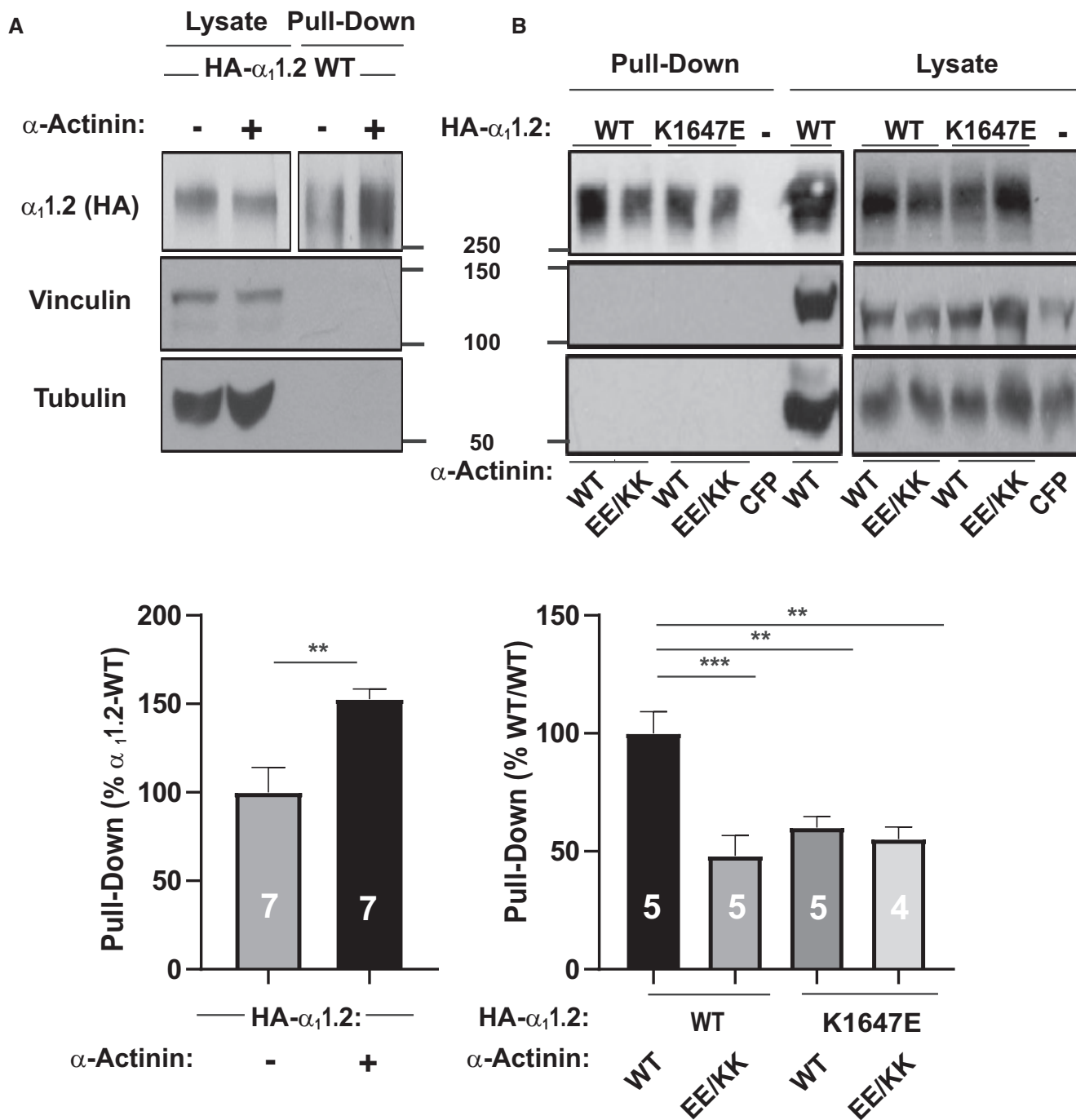


**Figure 6. Modulation of  $Ca_v1.2$  surface expression via its interaction with  $\alpha$ -actinin-1.**

**A** HEK293 cells were transfected with WT  $\alpha_1.2$ ,  $\alpha_2\delta-1$ , and  $\beta_{2A}$   $\pm$  WT  $\alpha$ -actinin-1 and cultured for 22–24 h before surface biotinylation. Shown are representative immunoblots of NeutrAvidin pull-down samples (from lysate containing 600  $\mu$ g protein) and total lysate samples containing 20  $\mu$ g protein.  $\alpha_1.2$  was detected with an antibody against its HA tag (top), which is present in all constructs used throughout this work. Pull-down and lysate samples are from the same blot but different exposures because signals from lysate samples were much stronger than from pull-down samples. Immunoblotting for vinculin (middle) and tubulin (bottom) indicated that comparable amounts of these intracellular control proteins were present in lysate samples. Their absence in pull-down samples as seen on the same blots showed that these prominent intracellular proteins did not undergo biotinylation as control for membrane integrity during surface biotinylation. Bar graph shows means  $\pm$  SEM of the pull-down immunosignals in mutants relative to surface labeling of control  $\alpha_1.2$  samples lacking  $\alpha$ -actinin-1 co-expression (mean set to 100%; see Materials and Methods; \*\* $P$  < 0.01 two-tailed  $t$ -test;  $n$  = 7).

**B** HEK293 cells were transfected with WT or K1647E mutant  $\alpha_1.2$ ,  $\alpha_2\delta-1$ , and  $\beta_{2A}$ , and WT or E847K/E851K mutant  $\alpha$ -actinin-1, or CFP alone as negative control and cultured for 22–24 h before surface biotinylation. Shown are representative immunoblots of pull-down and lysate samples as in (A). Bar graph shows means  $\pm$  SEM of the pull-down immunosignals in mutants relative to surface labeling in the WT/WT control (mean set to 100%; see Materials and Methods). \*\* $P$  < 0.01, \*\*\* $P$  < 0.001; one-way ANOVA with Tukey post hoc test;  $n$  = 4–5).

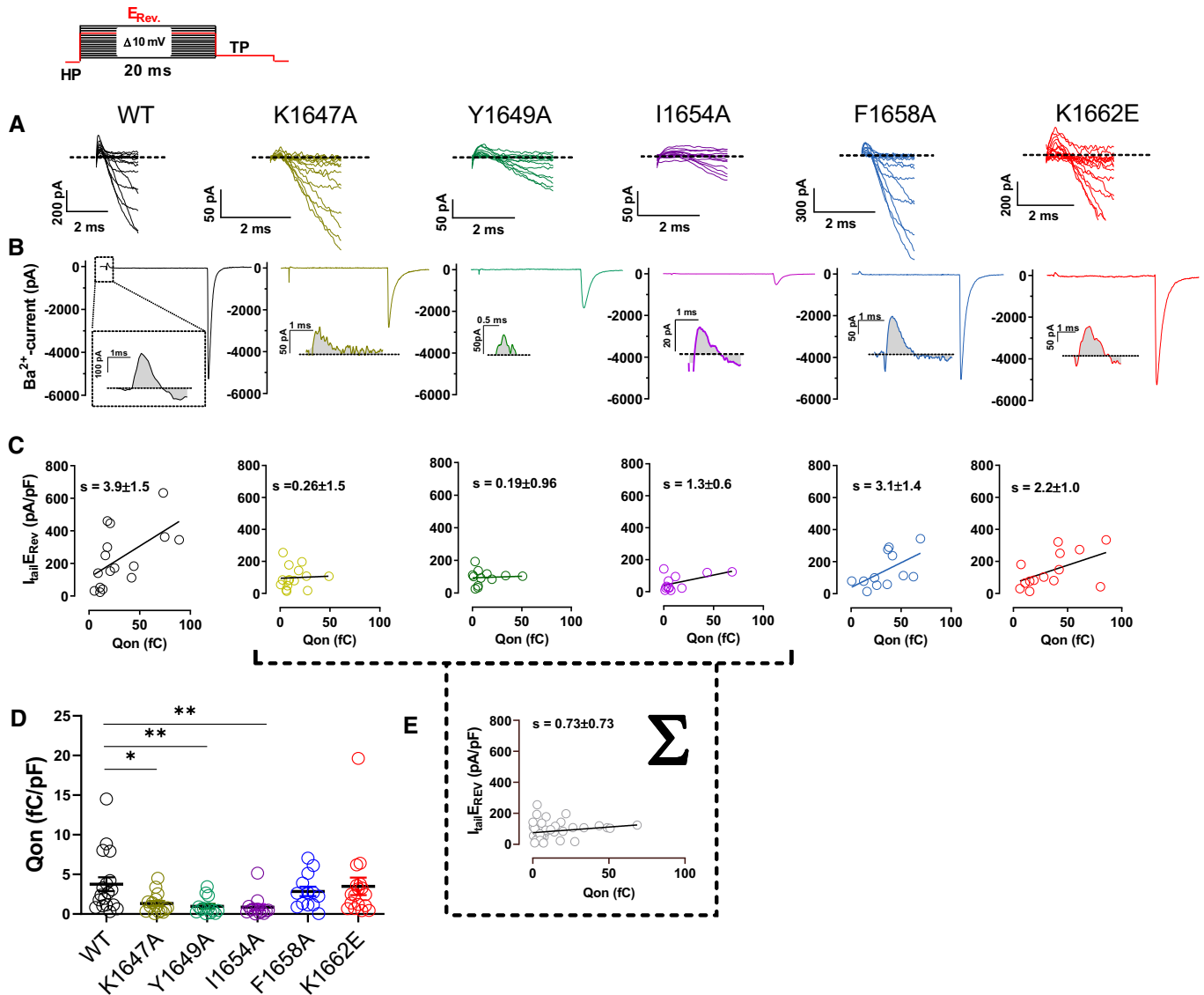


**Figure 7. Ca<sub>v</sub>1.2 mutations that affect  $\alpha$ -actinin-1 impair gating charge movement and its coupling to channel opening.**

HEK293 cells were transfected with  $\alpha_1$ 1.2,  $\alpha_2\delta$ -1, and  $\beta_{2A}$  before whole-cell patch recording in 20 mM Ba<sup>2+</sup>.

- A** Representative current traces of the first 2 ms obtained from recordings upon depolarizations from a holding potential of  $-80$  mV to the indicated potentials (the voltage protocol is schematized in the upper left corner).
- B** Representative current traces upon step depolarizations to the reversal potential ( $E_{rev}$ ) for 20 ms to obtain movement of the ON-gating charges ( $Q_{on}$ ), and subsequent to  $-50$  mV for 10 ms to obtain tail currents ( $I_{tail}$ ). Insets: magnifications of exemplary  $Q_{on}$  for Ca<sub>v</sub>1.2 WT, K1647A, Y1649A, I1654A, F1658A, and K1662E.
- C** Plots of  $I_{tail}$  (in this panel corrected for variations in cell capacitance) versus total detectable charge transfer for  $Q_{on}$ . Slopes of regression curves are strongly reduced for Ca<sub>v</sub>1.2 K1647A, Y1649A, and I1654A versus WT (see Table 7 for more details).
- D** Dot plots and means  $\pm$  SEM of  $Q_{on}$  (in this panel corrected for variations in cell capacitance; \* $P < 0.05$ ; \*\* $P < 0.01$ ; one-way ANOVA with Bonferroni post hoc test;  $n = 13$ –18; see Table 7 for more details).
- E** The reduction in slope of the regression curve of combined population data for K1647A, Y1649A, and I1654A versus WT indicates reduced coupling of  $I_{tail}$  with  $Q_{on}$  when  $\alpha$ -actinin binding to the IQ motif is diminished.

intersect to facilitate channel gating, possibly through similar effects on overall conformations of Ca<sub>v</sub>1.2.

All three  $\alpha$ -actinin binding-deficient IQ mutants of Ca<sub>v</sub>1.2 reduced NPo by  $\sim 90\%$  when channel density was reduced by only 35–40% as seen by surface labeling (Tseng *et al*, 2017). To further ascertain that a large portion of the reduction in NPo is due to a reduction in Po and not just N, i.e., not only due to a reduction in

surface expression, we determined the 95% confidence intervals (CIs) for surface biotinylation and surface labeling with antibodies with subsequent analysis by fluorescence-activated cell sorting (Bourdin *et al*, 2010; Yang *et al*, 2010), Po, and  $Q_{on}$  (Appendix Tables S1–S3). The CIs for surface biotinylation and surface antibody labeling are remarkably similar (e.g., 52–69% and 51–71%, respectively, for the most relevant mutant K1647A, with

WT being 100%) and overlap not at all with  $Q_{on}$  and  $Po$  (26–44% and 6–10%, respectively, for K1647A, with WT again being 100%). Thus, the CIs for the 95% CIs for reductions are ~29–49% for surface stainings, 56–74% for  $Q_{on}$ , and 90–94% for  $Po$ . Accordingly, it appears extremely unlikely that the reductions in surface expression can fully account for the reductions in  $Q_{on}$  and  $Po$  for  $\alpha$ -actinin binding-deficient Cav1.2; rather, loss of surface localization is only responsible for a fraction of the reductions in  $Q_{on}$  and  $Po$ . Similarly, the reduction in  $Q_{on}$  can most likely only partially account for the reduction in  $Po$ , supporting the notion that coupling between the movement of the voltage sensor and the channel gate is impaired in addition to the movement of this sensor.

If loss of  $\alpha$ -actinin binding to the IQ motif would not affect  $Po$  of individual channels, then  $NPo$  of all  $\alpha$ -actinin binding-deficient IQ mutants should be ~60% of wild-type Cav1.2. A 90% decrease in  $NPo$  means that 60% of the Cav1.2 channels that remain on the cell surface upon impairment of  $\alpha$ -actinin binding carry only ~10% of the current seen for the wild-type Cav1.2 population. These effects translate into a sixfold reduction in  $Po$  of individual Cav1.2 channels upon loss of  $\alpha$ -actinin binding.

Together with earlier work that showed that  $\alpha$ -actinin increases surface localization and postsynaptic accumulation of Cav1.2 (Hall et al, 2013; Tseng et al, 2017), this new work now demonstrates that  $\alpha$ -actinin serves a dual role in regulating Cav1.2 function. It not only promotes Cav1.2 surface expression but, remarkably, also exerts a strong positive effect on  $Po$ . This mechanism allows Cav1.2 to be minimally active during secretory trafficking or when it is outside its target regions but to become functionally fully engaged when anchored at proper locations such as postsynaptic sites. Thus, coupling of  $\alpha$ -actinin binding to both localization and activity of Cav1.2 is perfectly fine-tuned. This mechanism is so far unique. Whether analogous mechanisms apply to other channels and especially other  $Ca^{2+}$  channels, which may require potent mechanisms to prevent inappropriate and potentially harmful  $Ca^{2+}$  flux from secretory compartments or at the wrong locations on the cell surface, is now an intriguing premise that will inspire future work.

## Materials and Methods

### NMR spectroscopy

Xenopus calmodulin was expressed in *E. coli* strain BL21(DE3) grown in LB medium (unlabeled proteins) or M9 media supplemented with  $^{15}NH_4Cl$  or  $^{15}NH_4Cl/^{13}C$ -glucose for single- or double-labeled proteins, respectively. Recombinant CaM was prepared as described previously (Zhang et al, 2012).

Human  $\alpha$ -actinin-1\_EF12 (residues 750–812) and  $\alpha$ -actinin-1\_EF34 (residues 822–893) were each subcloned into pET3b vector and expressed in *E. coli* strain BL21(DE3) grown in LB medium (unlabeled proteins) or M9 media supplemented with  $^{15}NH_4Cl$  or  $^{15}NH_4Cl/^{13}C$ -glucose for single- or double-labeled proteins, respectively.  $\alpha$ -actinin-1\_EF12 and  $\alpha$ -actinin-1\_EF34 were each purified and prepared as described (Turner et al, 2016).

Unlabeled Cav1.2 IQ peptide (residues 1,644–1,664) was purchased from ChinaPeptides. The peptide was dissolved in d6-DMSO to give a peptide concentration of 7.8 mM. An aliquot of

peptide (1.5 equivalents) was added to a dilute solution of  $\alpha$ -actinin-1\_EF34 or apoCaM (50  $\mu$ M protein dissolved in 20 mM 2-amino-2-hydroxymethyl-propane-1,3-diol-d11 (Tris- $d_{11}$ ) with 50 mM NaCl, 5 mM dithiothreitol-d10 (DTT- $d_{10}$ ), and 95%  $H_2O$ /5%  $D_2O$ ) and incubated at 15°C for 1 h to ensure complete binding of the peptide. The complex was then concentrated to a final concentration of 500  $\mu$ M in a final volume of 500  $\mu$ l for NMR experiments.

### Production and use of isotope-labeled peptides using pET-31

We expressed  $^{15}N$ - or  $^{15}N/^{13}C$ -labeled IQ peptide in *E. coli* as a fusion protein with the ketosteroid isomerase (KSI) using the pET31 plasmid (Kuliopulos et al, 1994) (Novagen/EMD Biosciences). KSI fusion proteins are concentrated in inclusion bodies in *E. coli*, protecting the fused peptide from proteolysis. The fusion protein was purified by affinity chromatography under denaturing conditions via a 6x-His tag at the C-terminus. To release the peptide of interest, the purified fusion is cleaved using cyanogen bromide (CNBr). The CNBr cleaves at methionine residues that were engineered between the KSI and peptide, and between the peptide and 6x-His tag. This cleavage mixture is then rotary evaporated to dryness and resuspended in an appropriate ratio of acetonitrile/water, which solubilizes primarily the peptide and not KSI. Finally, the peptide is purified by reverse-phase HPLC.

Two complementary oligonucleotides that code for Cav1.2 IQ peptide (5'-p-TTT TAT GCG ACC TTT CTG ATT CAG GAA TAT TTT CGC AAA TTT AAA AAA CGC AAA ATG; 5'-p-TTT GCG TTT TTT AAA TTT GCG AAA ATA TTC CTG AAT CAG AAA GGT CGC ATA AAA CAT) were annealed in 40 mM Tris-HCl, pH 8.0, 10 mM  $MgCl_2$ , and 50 mM NaCl by heating to 95°C and then cooling slowly (> 2 h) to room temperature (RT). The annealed, double-stranded insert was then ligated into AlwNI-digested and dephosphorylated pET31 using T4 DNA ligase. The 5'-phosphorylation augments ligation, and the extra Met codons (underlined) provide compatible sticky ends for the AlwNI-cut plasmid as well as the sites of CNBr cleavage. 2  $\mu$ l of the ligation mixture was transformed into DH5 alpha cells and plasmids from individual ampicillin-resistant colonies sequenced. Successful insertions were obtained, including some multiple insertions. We used one of the single-insertion plasmids for expression in M9 minimal media. *E. coli* was lysed by sonication. The insoluble material was collected by ultracentrifugation and resuspended in 6M guanidine, insoluble material removed by ultracentrifugation, and the supernatant loaded onto a Ni-NTA column equilibrated with 6M guanidine buffer. After elution with 300 mM imidazole, the purified fractions were pooled and then dialyzed against ultrapure water, causing the fusion protein to precipitate. Precipitate was collected by centrifugation and resuspended in 80% formic acid, transferred to a round-bottom flask, and injected with  $N_2$  at ~3 psi. For a 2L scale expression, we used 60 ml of formic acid solution and added 2 g of solid CNBr to start the cleavage reaction. After overnight reaction, the flask was roto-evaporated to dryness. The clear peptide film was resuspended in 40% acetonitrile/60%  $H_2O$  and mixed for > 1 h. After centrifugation to remove any insoluble material, the supernatant was lyophilized, resuspended in  $H_2O$  + 0.1% trifluoroacetic acid, and run over a C18 reverse-phase HPLC column using a gradient of 9–28% acetonitrile. Peak fractions were collected, lyophilized, and analyzed by MALDI-MS to identify

the desired peptide product. Dry fractions of peptide were resolubilized in DMSO-d<sub>6</sub> to a concentration of > 5 mM.

To measure residual dipolar couplings (RDCs) of  $\alpha$ -actinin-1\_EF34 or apoCaM bound to IQ peptide, the filamentous bacteriophage Pf1 (Asla Biotech Ltd., Latvia) was used as an orienting medium. Pf1 (12 mg/ml) was added to <sup>15</sup>N-labeled  $\alpha$ -actinin-1\_EF34 or apoCaM bound to unlabeled IQ at pH 7.0, to produce weak alignment of the complex.

#### Haddock structure determination of $\alpha$ -actinin-1/IQ or apoCaM/IQ

The molecular docking of  $\alpha$ -actinin-1 and apoCaM to the Ca<sub>v</sub>1.2 IQ motif (residues 1,644–1,664) was performed using the Haddock d-level 2.2 web server as described (van Zundert *et al*, 2016). Residual dipolar couplings, chemical shift perturbation, and mutagenesis data were used as structural restraints. For active restraints or ambiguous interaction restraints (AIRs), chemical shift perturbation was used, selecting residues whose chemical shift perturbation falls above the average perturbation.

The initial docking calculation used NMR-derived structures of  $\alpha$ -actinin-1 or apoCaM as determined in this study, which were each docked with the helical structure of Ca<sub>v</sub>1.2 IQ peptide (residues 1,644–1,664) (Van Petegem *et al*, 2005) as input structures for Haddock. A total of 69 and 42 AIR restraints were used for  $\alpha$ -actinin-1 and apoCaM, respectively, based on chemical shift perturbation data, and 16 active restraints were used for the IQ peptide from chemical shift perturbation. Unambiguous restraints were introduced to define key intermolecular interactions (IQ K1647- $\alpha$ -actinin-1\_EF34 E847; IQ K1647- $\alpha$ -actinin-1\_EF34 E851; IQ K1662-CaM E88; IQ I1654- $\alpha$ -actinin-1\_EF3/4F833; and IQ I1654-apoCaM F90), which were each verified by mutagenesis (Tables 2 and 4).

Initial docking calculations used AIRs based on chemical shift perturbation data, and the top 200 structures were selected for simulated annealing and water refinement. The lowest energy structures were then run again, adding unambiguous restraints based on mutagenesis data. Rigid-body docking, simulated annealing, and water refinement were run using the top 200 structures. RDC restraints assigned to  $\alpha$ -actinin-1 and apoCaM were then added using the Sani statement, with tensor values Dr and Da calculated using the program PALES (Zweckstetter, 2008). A total of 74 RDC values were used from residues found in regions of regular secondary structure and as deemed reliable by the PALES calculation.

#### Fluorescence polarization (FP) assays

Fluorescein-labeled peptides (100 nM; ChinaPeptides, Shanghai, China) were titrated with increasing concentrations of either purified  $\alpha$ -actinin-1 or CaM in FP buffer (50 mM HEPES, pH 7.4, 100 mM KCl, 1 mM MgCl<sub>2</sub>, 0.05 mM EGTA, 5 mM nitrilotriacetic acid) and FP determined with a Synergy 2 plate reader (BioTek, Winooski, VT) as described (Zhang *et al*, 2014; Patriarchi *et al*, 2016; Tseng *et al*, 2017). FP was calculated as  $P = (I_v - g \cdot I_h) / (I_v + g \cdot I_h)$ ;  $I_v$  is vertical and  $I_h$  is horizontal fluorescence intensity, respectively, and  $g$  is the correction factor for fluorescein. To obtain binding curves and  $K_d$  values, data were fitted in GraphPad Prism 5 to the equation  $Y = B \cdot X / (K_d + X)$ ;  $B$  is maximal FP value that would

be reached at saturation as determined by extrapolation of the fitted curve.

#### Isothermal titration calorimetry

ITC experiments were performed using a VP-ITC calorimeter (MicroCal) at 27°C, and data were acquired and processed with MicroCal software as described previously (Wingard *et al*, 2005). Samples of apoCaM (injectant) and IQ (titrant) were prepared by exchanging each into buffer containing 50 mM HEPES, pH 7.4, 100 mM NaCl, 0.05 mM EGTA, and 1 mM MgCl<sub>2</sub>. The IQ peptide in the sample cell (10  $\mu$ M, 1.5 ml) was titrated with apoCaM (100  $\mu$ M) using 35 injections of 10  $\mu$ l each.

#### Expression of Ca<sub>v</sub>1.2 and $\alpha$ -actinin-1 in HEK293 cells

HEK293T/17 cells were maintained in DMEM-10 [Dulbecco's modified Eagle's medium (Life Technologies) supplemented with 10% fetal bovine serum (FBS, Atlanta Biologicals)] at 37°C in humidified incubators injected with 5% CO<sub>2</sub> and 95% air (Tseng *et al*, 2017). For expression of Ca<sub>v</sub>1.2, HEK293T/17 cells were transfected with rat  $\alpha_1$ 1.2 (GenBank ID: M67515.1) cDNA subcloned into pECFP-C1 vector (Tseng *et al*, 2017) encoding an in-frame N-terminally fused eCFP tag and an HA tag in the S5-H5 extracellular loop of domain II (Green *et al*, 2007), which does not affect channel properties (Altier *et al*, 2002). The point mutations in plasmids encoding single-residue K1647A, K1647E, F1648A, Y1649A, I1654A, F1658A, and K1662E exchanges in  $\alpha_1$ 1.2 were generated via QuikChange II using the above pECFP-C1 rat  $\alpha_1$ 1.2 plasmid DNA as template as described (Tseng *et al*, 2017) and the oligonucleotides described in Appendix Table S4. For full expression of Ca<sub>v</sub>1.2, cells were also co-transfected with pGWIH-based plasmids encoding the auxiliary subunits rat  $\beta_{2A}$  (Perez-Reyes *et al*, 1992) and rabbit  $\alpha_2\delta$ -1 (Ellis *et al*, 1988). To assess the contributions of  $\alpha$ -actinin-1 on Ca<sub>v</sub>1.2, cells were transfected with pCMV plasmid DNAs encoding WT (Hall *et al*, 2013) or mutant  $\alpha$ -actinin-1. The K847E/K851EE point mutations in  $\alpha$ -actinin-1 were produced via QuikChange II mutagenesis as before (Tseng *et al*, 2017). The forward primer for making the K851E mutation, which was performed first, was 5'p-CCA TGG ACA AAT TGC GCA GAA AGC TGC CAC CCG ACC AGG and reverse primer 5'p-CCT GGT CGG GTG GCA GCT TTC TGC GCA ATT TGT CCA TGG. Forward primer for the K847E mutation was 5'p-GAA CTA CAT TAC CAT GAA CAA ATT GCG CCG CGA GCT GCC ACC C and reverse primer 5'p-GGG TGG CAG CTC GCG GCG CAA TTT GTC CAT GGT AAT GTA GTT C. Transfection of HEK293T/17 cells was accomplished using Ca<sup>2+</sup> phosphate precipitation (Tseng *et al*, 2017) for single-channel recording and surface labeling or Lipofectamine 2000 for the analysis of Q<sub>on</sub>.

#### Cell surface biotinylation assays

Seven hours after transfection, cells were washed once with 150 mM NaCl, 10 mM NaHCO<sub>2</sub>, pH 7.4 (PBS) and cultured for another 15–17 h in fresh medium. 22–24 h after transfection, cells were either harvested, monodispersed (> 95% viability), and then labeled with EZ-link-sulfo-NHS-LC-biotin (Thermo Fisher Scientific) in solution essentially as described (Tseng *et al*, 2017) or directly labeled while adhered to the petri dish. In the latter case, adherent cells on the dish were washed twice with ice-cold PBS containing



0.5 mM  $Mg^{2+}$  and 1 mM  $Ca^{2+}$  and incubated on ice with PBS containing 0.4 mg/ml EZ-link-sulfo-NHS-LC-biotin for 15 min. The labeling reaction was quenched by three 5-min washes with 40 mM glycine in PBS containing 0.5 mM  $Mg^{2+}$  and 1 mM  $Ca^{2+}$  on ice. Cells were harvested by scraping in PBS and collected by centrifugation. Cell pellets were lysed in ice-cold RIPA buffer (50 mM Tris-HCl, pH 7.4, 150 mM NaCl, 5 mM EGTA, 10 mM EDTA, 1% NP-40, 0.05% SDS, 0.4% DOC, and 10% glycerol) supplemented with a cocktail of protease inhibitors (1  $\mu$ g/ml leupeptin (Merck Millipore), 2  $\mu$ g/ml aprotinin (Merck Millipore), 1  $\mu$ g/ml pepstatin A (Merck Millipore), and 34  $\mu$ g/ml phenylmethanesulfonyl fluoride (PMSF; Sigma)). The solubilized material was cleared of insoluble debris by centrifugation at 200,000 $\times$  *g* for 30 min at 4°C. Biotinylated constituents in 600  $\mu$ g of cell protein lysate were affinity purified by incubation with 30  $\mu$ l of NeutrAvidin-conjugated Sepharose beads (Thermo Fisher Scientific) for 2 h at 4°C. Bead-bound material was collected by centrifugation and washed three times with ice-cold buffer, and immobilized proteins were extracted in SDS sample buffer. Proteins were fractionated by SDS-PAGE in 7.5% acrylamide gels and transferred onto polyvinylidene difluoride (PVDF; Bio-Rad) membranes. PVDF membranes were incubated in blocking buffer (BB) consisting of 150 mM NaCl, 10 mM Tris-HCl, pH 7.4 (TBS) with 0.10% Tween (TBST), and 2% bovine serum albumin (BSA; RPI Corp.) for 1 h at RT before incubation with primary antibodies in BB for 3 h at RT.  $\alpha_1.2$  was detected by antibodies against the HA tag and, for confirmation, the intracellular loop II/III FP1 epitope (Buonarati *et al*, 2017) and the CNC2 epitope near the C-terminus of  $\alpha_1.2$  (Buonarati *et al*, 2017). Probing with antibodies against the cytosolic protein vinculin (Cell Signaling Technologies) and  $\alpha$ -tubulin (Santa Cruz Biotechnology) was used to correct for variation in protein content in lysates and as negative control for surface biotinylation. Membranes were washed for 40 min with at least five exchanges of TBST, incubated with horseradish peroxidase-conjugated secondary goat anti-mouse antibodies (HA,  $\alpha$ -tubulin; Jackson) or mouse anti-rabbit antibodies (FP1, CNC2, vinculin; Jackson) for 1 h at RT, and washed again with TBST with at least five exchanges for 1.5 h. Immunosignals were detected using the horseradish peroxidase substrates Luminata Classico or Crescendo (Merck Millipore) or Femto (Thermo Fisher Scientific) by X-ray film (Denville Scientific Inc.). Multiple exposures over increasing time periods were taken to ensure that all signals were in the linear range (Davare & Hell, 2003; Hall *et al*, 2006). Films were scanned and assessed via ImageJ to determine signal intensity for each band. Background signals in individual lanes were subtracted from the band signal before further analysis. To correct differences in immunosignal strengths due to potential differences during immunoblotting and film exposures between experiments, the individual immunosignals for each  $\alpha_1.2$  pull-down sample were divided by the sum of all immunosignals from one blot to obtain the relative signal fraction for each band (Degaspero *et al*, 2014). The mean of the WT control signals from all experiments was then calculated and all fractional values from all samples (WT and mutants) divided by this value (the WT mean transforms to 1 with this algorithm) (Degaspero *et al*, 2014). All values were then converted to percent, with the mean of WT control equaling 100%. The data were statistically analyzed applying either a Student's *t*-test (two-sample comparison) or ANOVA with Bonferroni's post hoc test as before (Tseng *et al*, 2017).

### Cell-attached Patch-Clamp recording

Cell-attached patch-clamp recordings were performed as before (Davare *et al*, 2001; Patriarchi *et al*, 2016; Qian *et al*, 2017) on an Olympus IX70-inverted microscope at room temperature (22°C). Recordings were obtained with an Axopatch 200B amplifier, and data were sampled at 10 kHz with a low-pass filter at 2 kHz (3 dB, four-pole Bessel) and digitalized with a Digidata 1440 digitizer. Recording electrodes were fabricated from borosilicate capillary glass (0.86 OD) with a Flaming micropipette puller (Model P-97, Sutter Instruments) and polished (polisher from World Precision Instruments; 3.5–6.5 M $\Omega$  resistance). The extracellular solution contained (in mM) 145 KCl, 10 NaCl, and 10 HEPES, pH 7.4 (NaOH). The high  $K^+$  concentration was used for optimal control of the transmembrane potential under the patch during depolarizations to 0 mV. The pipette solution contained (in mM) 20 tetraethylammonium chloride (TEA-Cl), 110 BaCl<sub>2</sub> (as charge carrier), and 10 HEPES, pH 7.3 (TEA-OH). Cells were depolarized from a holding potential of –80 mV to 0 mV every 5 s. Event lists were translated from raw Ba<sup>2+</sup> currents after leak, and capacity transients were digitally subtracted. Data were analyzed based on the half-height criterion (Sachs *et al*, 1982) with the single-channel software provided by pClamp 10. The number of channels (*k*) in the patch was estimated based on the observed simultaneous and stacked openings over several minutes at the depolarizing test potential (Herzig *et al*, 2007; Bartels *et al*, 2018). The *k*-value is then determined by the observed maximum current amplitude divided by the unitary current amplitude. Data with more than > 3 channels (*k* > 3) in the patch were not considered for statistical analysis in order to prevent overinterpretation of channel open probability. For statistical analysis, single-channel parameters were corrected by the channel number as previously (Schroder *et al*, 1998; Bartels *et al*, 2009). For a sufficient statistical analysis, 50–100 Ba<sup>2+</sup> current traces were recorded on average for each cell for each experimental condition.

### Whole-cell patch-clamp recordings

Whole-cell patch-clamp recordings were performed as before (Bartels *et al*, 2018) on an Olympus IX70-inverted microscope at room temperature (22°C). Macroscopic Ba<sup>2+</sup> currents ( $I_{Ba}$ ) of Ca<sub>v</sub>1.2 were recorded in external solution containing (in mM) 75 CsCl, 40 TEA-Cl, 20 BaCl<sub>2</sub>, 1 MgCl<sub>2</sub>, 10 HEPES, and 10 glucose with a pH adjusted to 7.2 (TEA-OH) and an osmolarity of 300–310 (sucrose). The internal pipette solution contained (in mM) 110 CsCl, 30 TEA-Cl, 1 MgCl<sub>2</sub>, 4 Mg-ATP, and 10 HEPES, pH 7.2 (CsOH), mOsm 290–300 (sucrose). Pipette resistance was usually between 1.7 and 2.5 M $\Omega$ . The series resistance and the cell capacitance were taken from an Axopatch 200B amplifier (Molecular Devices) and compensated not more than < 40% in order to prevent current oscillation. On-gating currents ( $I_{on}$ ) were sampled at 50 kHz and low-pass-filtered at 5 kHz and further quantified through current integration over the first 2–3 ms of the beginning of the test pulse. Cells were clamped at a holding potential of –80 mV and depolarized by a 20 ms test pulse of a series of activating potentials starting from –60 mV to +80 mV to determine the reversal potential ( $E_{rev}$ ). Tail currents ( $I_{tail}$ ) were then measured after repolarization to –50 mV for 10 ms. Recorded data were leak and capacity corrected with an online *P/4*

protocol. The liquid junction potential was not considered for correction in the experiment. Data acquisition and analysis were obtained with pClamp 10. Curve fitting was performed by using GraphPad Prism VIII software (San Diego).

## Data availability

The NMR assignments have been deposited in the BMRB (accession number 25902; <http://www.bmrwisc.edu/>). The atomic coordinates have been deposited into the Protein Databank (6COA and 6CTB).

**Expanded View** for this article is available online.

## Acknowledgements

We thank Dr. Elza Kuzmenkina (University of Cologne, Germany) for providing the coding of the algorithm for calculating assembly averages. This work was supported by NIH grants T32 GM113770 (AMC), T32 GM099608 (PBH), R01 HL098200 (MFN), R01 HL121059 (MFN), R01 EY012347 (JBA), R01MH097887 (JWH), R01 AG017502 (JWH), R01 NS078792 (JWH), and the American Heart Association (AHA) Predoctoral Fellowship AHA 14PRE19900021 (PBH).

## Author contributions

MT, DEA, MN-C, PB, KNMM, P-YT, MFN, MCH, JBA, and JWH designed experiments; MT, DEA, MN-C, PB, AMC, KNMM, PBH, P-YT, MFN, and MCH performed experiments; MT, DEA, MN-C, PB, AMC, PBH, VY-Y, DMB, MFN, MCH, JBA, and JWH analyzed data; and MT, DEA, MN-C, PB, VY-Y, DMB, MFN, MCH, JBA, and JWH wrote the manuscript.

## Conflict of interest

The authors declare that they have no conflict of interest.

## References

- Adams PJ, Ben-Johny M, Dick IE, Inoue T, Yue DT (2014) Apocalmodulin itself promotes ion channel opening and Ca(2+) regulation. *Cell* 159: 608–622
- Alexander KA, Cimler BM, Meier KE, Storm DR (1987) Regulation of calmodulin binding to P-57. A neurospecific calmodulin binding protein. *J Biol Chem* 262: 6108–6113
- Altier C, Dubel SJ, Barrere C, Jarvis SE, Stotz SC, Spaetgens RL, Scott JD, Cornet V, De Waard M, Zamponi GW et al (2002) Trafficking of L-type calcium channels mediated by the postsynaptic scaffolding protein AKAP79. *J Biol Chem* 277: 33598–33603
- Atkinson RA, Joseph C, Kelly G, Muskett FW, Frenkiel TA, Nietlispach D, Pastore A (2001) Ca<sup>2+</sup>-independent binding of an EF-hand domain to a novel motif in the alpha-actinin-titin complex. *Nat Struct Biol* 8: 853–857
- Backman L (2015) Calcium affinity of human alpha-actinin 1. *PeerJ* 3: e944
- Bartels P, Behnke K, Michels G, Groner F, Schneider T, Henry M, Barrett PQ, Kang HW, Lee JH, Wiesen MH et al (2009) Structural and biophysical determinants of single Ca(V)3.1 and Ca(V)3.2 T-type calcium channel inhibition by N(2)O. *Cell Calcium* 46: 293–302
- Bartels P, Yu D, Huang H, Hu Z, Herzig S, Soong TW (2018) Alternative splicing at N terminus and domain I modulates Cav1.2 inactivation and surface expression. *Biophys J* 114: 2095–2106
- Ben Johny M, Yang PS, Bazzazi H, Yue DT (2013) Dynamic switching of calmodulin interactions underlies Ca<sup>2+</sup> regulation of Cav1.3 channels. *Nat Commun* 4: 1717
- Ben-Johny M, Yang PS, Niu J, Yang W, Joshi-Mukherjee R, Yue DT (2014) Conservation of Ca(2+)/calmodulin regulation across Na and Ca(2+) channels. *Cell* 157: 1657–1670
- Berkefeld H, Sailer CA, Bildl W, Rohde V, Thumfart JO, Eble S, Klugbauer N, Reisinger E, Bischofberger J, Oliver D et al (2006) BKCa-Cav channel complexes mediate rapid and localized Ca<sup>2+</sup>-activated K<sup>+</sup> signaling. *Science* 314: 615–620
- Berman DE, Dudai Y (2001) Memory extinction, learning anew, and learning the new: dissociations in the molecular machinery of learning in cortex. *Science* 291: 2417–2419
- Bourdin B, Marger F, Wall-Lacelle S, Schneider T, Klein H, Sauve R, Parent L (2010) Molecular determinants of the Cavbeta-induced plasma membrane targeting of the Cav1.2 channel. *J Biol Chem* 285: 22853–22863
- Buonarati OR, Henderson PB, Murphy GG, Horne MC, Hell JW (2017) Proteolytic processing of the L-type Ca<sup>2+</sup> channel alpha 1.2 subunit in neurons. *FL000 Res* 6: 1166
- Cahill L, Prins B, Weber M, McGaugh JL (1994) Beta-adrenergic activation and memory for emotional events. *Nature* 371: 702–704
- Carter ME, Yizhar O, Chikahisa S, Nguyen H, Adamantidis A, Nishino S, Deisseroth K, de Lecea L (2010) Tuning arousal with optogenetic modulation of locus coeruleus neurons. *Nature Neurosci* 13: 1526–1533
- Chagot B, Chazin WJ (2011) Solution NMR structure of Apo-calmodulin in complex with the IQ motif of human cardiac sodium channel Nav1.5. *J Mol Biol* 406: 106–119
- Cimler BM, Andreassen TJ, Andreassen KI, Storm DR (1985) P-57 is a neural specific calmodulin-binding protein. *J Biol Chem* 260: 10784–10788
- Cohen SM, Suutari B, He X, Wang Y, Sanchez S, Tirko NN, Mandelberg NJ, Mullins C, Zhou G, Wang S et al (2018) Calmodulin shuttling mediates cytonuclear signaling to trigger experience-dependent transcription and memory. *Nat Commun* 9: 2451
- Dai S, Hall DD, Hell JW (2009) Supramolecular assemblies and localized regulation of voltage-gated ion channels. *Physiological Rev* 89: 411–452
- Davare MA, Avdonin V, Hall DD, Peden EM, Burette A, Weinberg RJ, Horne MC, Hoshi T, Hell JW (2001) A beta2 adrenergic receptor signaling complex assembled with the Ca<sup>2+</sup> channel Cav1.2. *Science* 293: 98–101
- Davare MA, Hell JW (2003) Increased phosphorylation of the neuronal L-type Ca(2+) channel Ca(v)1.2 during aging. *Proc Natl Acad Sci USA* 100: 16018–16023
- Degasperi A, Birtwistle MR, Volinsky N, Rauch J, Kolch W, Kholodenko BN (2014) Evaluating strategies to normalise biological replicates of Western blot data. *PLoS ONE* 9: e87293
- Dolmetsch RE, Pajvani U, Fife K, Spotts JM, Greenberg ME (2001) Signaling to the nucleus by an L-type calcium channel-calmodulin complex through the MAP kinase pathway. *Science* 294: 333–339
- Dolphin AC (2012) Calcium channel auxiliary alpha(2)delta and beta subunits: trafficking and one step beyond. *Nature Rev Neurosci* 13: 542–555
- Dolphin AC (2016) Voltage-gated calcium channels and their auxiliary subunits: physiology and pathophysiology and pharmacology. *J Physiol* 594: 5369–5390
- Egrie JC, Campbell JA, Flangas AL, Siegel FL (1977) Regional, cellular and subcellular distribution of calcium-activated cyclic nucleotide phosphodiesterase and calcium-dependent regulator in porcine brain. *J Neurochem* 28: 1207–1213
- Ellis SB, Williams ME, Ways NR, Brenner R, Sharp AH, Leung AT, Campbell KP, McKenna E, Koch WJ, Hui A et al (1988) Sequence and expression of mRNAs encoding the alpha<sub>1</sub> and alpha<sub>2</sub> subunits of the DHP-sensitive calcium channel. *Science* 241: 1661–1664

- Evans TI, Hell JW, Shea MA (2011) Thermodynamic linkage between calmodulin domains binding calcium and contiguous sites in the C-terminal tail of Ca(V)1.2. *Biophys Chem* 159: 172–187
- Feldkamp MD, Yu L, Shea MA (2011) Structural and energetic determinants of apo calmodulin binding to the IQ motif of the Na(V)1.2 voltage-dependent sodium channel. *Structure* 19: 733–747
- Findeisen F, Rumpf CH, Minor DL Jr (2013) Apo states of calmodulin and CaBP1 control Cav1 voltage-gated calcium channel function through direct competition for the IQ domain. *J Mol Biol* 425: 3217–3234
- Fuller MD, Emrick MA, Sadilek M, Scheuer T, Catterall WA (2010) Molecular mechanism of calcium channel regulation in the fight-or-flight response. *Sci Signal* 3: ra70
- Fuller MD, Fu Y, Scheuer T, Catterall WA (2014) Differential regulation of Cav1.2 channels by cAMP-dependent protein kinase bound to A-kinase anchoring proteins 15 and 79/150. *J Gen Physiol* 143: 315–324
- Gabelli SB, Boto A, Kuhns VH, Bianchet MA, Farinelli F, Aripirala S, Yoder J, Jakoncic J, Tomaselli GF, Amzel LM (2014) Regulation of the NaV1.5 cytoplasmic domain by calmodulin. *Nat Commun* 5: 5126
- Gabelli SB, Yoder JB, Tomaselli GF, Amzel LM (2016) Calmodulin and Ca(2+) control of voltage gated Na(+) channels. *Channels* 10: 45–54
- Ghosh D, Syed AU, Prada MP, Nystoriak MA, Santana LF, Nieves-Cintrón M, Navedo MF (2017) Calcium channels in vascular smooth muscle. *Adv Pharmacol* 78: 49–87
- Ghosh D, Nieves-Cintrón M, Tajada S, Brust-Mascher I, Horne MC, Hell JW, Dixon RE, Santana LF, Navedo MF (2018) Dynamic L-type Cav1.2 channel trafficking facilitates Cav1.2 clustering and cooperative gating. *Biochim Biophys Acta Mol Cell Res* 1865: 1341–1355
- Green EM, Barrett CF, Bultynck G, Shamah SM, Dolmetsch RE (2007) The tumor suppressor e1F3e mediates calcium-dependent internalization of the L-type calcium channel Cav1.2. *Neuron* 55: 615–632
- Grover LM, Teyler TJ (1990) Two components of long-term potentiation induced by different patterns of afferent activation. *Nature* 347: 477–479
- Hall DD, Feekes JA, Arachchige Don AS, Shi M, Hamid J, Chen L, Strack S, Zamponi GW, Horne MC, Hell JW (2006) Binding of protein phosphatase 2A to the L-type calcium channel Cav1.2 next to Ser 1928, its main PKA site, is critical for Ser1928 dephosphorylation. *Biochemistry* 45: 3448–3459
- Hall DD, Dai S, Tseng P-Y, Malik ZA, Nguyen M, Matt L, Schnitzler K, Shephard A, Mohapatra D, Tsuruta F et al (2013) Competition between  $\alpha$ -Actinin and Ca<sup>2+</sup>-calmodulin controls surface retention of the L-type Ca<sup>2+</sup> channel Cav1.2. *Neuron* 78: 483–497
- Hell JW, Yokoyama CT, Wong ST, Warner C, Snutch TP, Catterall WA (1993) Differential phosphorylation of two size forms of the neuronal class C L-type calcium channel  $\alpha$ 1 subunit. *J Biol Chem* 268: 19451–19457
- Hell JW (2014) CaMKII: claiming center stage in postsynaptic function and organization. *Neuron* 81: 249–265
- Herzig S, Khan IF, Grundemann D, Matthes J, Ludwig A, Michels G, Hoppe UC, Chaudhuri D, Schwartz A, Yue DT et al (2007) Mechanism of Ca(v)1.2 channel modulation by the amino terminus of cardiac beta2-subunits. *FASEB J* 21: 1527–1538
- Houdusse A, Gaucher JF, Kremontsova E, Mui S, Trybus KM, Cohen C (2006) Crystal structure of apo-calmodulin bound to the first two IQ motifs of myosin V reveals essential recognition features. *Proc Natl Acad Sci USA* 103: 19326–19331
- Hovey L, Fowler CA, Mahling R, Lin Z, Miller MS, Marx DC, Yoder JB, Kim EH, Tefft KM, Waite BC et al (2017) Calcium triggers reversal of calmodulin on nested anti-parallel sites in the IQ motif of the neuronal voltage-dependent sodium channel NaV1.2. *Biophys Chem* 224: 1–19
- Hu H, Real E, Takamiya K, Kang MG, Ledoux J, Huganir RL, Malinow R (2007) Emotion enhances learning via norepinephrine regulation of AMPA-receptor trafficking. *Cell* 131: 160–173
- Huang KP, Huang FL, Li J, Schuck P, McPhee P (2000) Calcium-sensitive interaction between calmodulin and modified forms of rat brain neurogranin/RC3. *Biochemistry* 39: 7291–7299
- Huang KP, Huang FL, Jager T, Li J, Reymann KG, Balschun D (2004) Neurogranin/RC3 enhances long-term potentiation and learning by promoting calcium-mediated signaling. *J Neurosci* 24: 10660–10669
- Iacobucci GJ, Popescu GK (2017) Resident calmodulin primes NMDA receptors for Ca(2+)-Dependent inactivation. *Biophys J* 113: 2236–2248
- Kuliopulos A, Nelson NP, Yamada M, Walsh CT, Furie B, Furie BC, Roth DA (1994) Localization of the affinity peptide-substrate inactivator site on recombinant vitamin K-dependent carboxylase. *J Biol Chem* 269: 21364–21370
- Li H, Pink MD, Murphy JG, Stein A, Dell'Acqua ML, Hogan PG (2012) Balanced interactions of calcineurin with AKAP79 regulate Ca<sup>2+</sup>-calcineurin-NFAT signaling. *Nat Struct Mol Biol* 19: 337–345
- Lian LY, Myatt D, Kitmitto A (2007) Apo calmodulin binding to the L-type voltage-gated calcium channel Cav1.2 IQ peptide. *Biochem Biophys Res Commun* 353: 565–570
- Ma H, Groth RD, Cohen SM, Emery JF, Li B, Hoedt E, Zhang G, Neubert TA, Tsien RW (2014) gammaCaMKII shuttles Ca(2+)/CaM to the nucleus to trigger CREB phosphorylation and gene expression. *Cell* 159: 281–294
- Man KNM, Navedo MF, Horne MC, Hell JW (2020)  $\beta_2$  adrenergic receptor complexes with the L-type Ca<sup>2+</sup> channel Cav1.2 and AMPA-type glutamate receptors: paradigms for pharmacological targeting of protein interactions. *Annu Rev in Pharmacol and Toxicol* 60: 29.1–29.20
- Marrion NV, Tavalin ST (1998) Selective activation of Ca<sup>2+</sup>-activated K<sup>+</sup> channels by co-localized Ca<sup>2+</sup> channels in hippocampal neurons. *Nature* 395: 900–905
- Matt L, Kim K, Hergarden AC, Patriarchi T, Malik ZA, Park DK, Chowdhury D, Buonarati OR, Henderson PB, Gokcek Sarac C et al (2018) alpha-actinin anchors PSD-95 at postsynaptic sites. *Neuron* 97: 1094–1109 e9
- Minzenberg MJ, Watrous AJ, Yoon JH, Ursu S, Carter CS (2008) Modafinil shifts human locus coeruleus to low-tonic, high-phasic activity during functional MRI. *Science* 322: 1700–1702
- Patriarchi T, Qian H, Di Biase V, Malik ZA, Chowdhury D, Price JL, Hammes EA, Buonarati OR, Westenbroek RE, Catterall WA et al (2016) Phosphorylation of Cav1.2 on S1928 uncouples the L-type Ca<sup>2+</sup> channel from the  $\beta_2$  adrenergic receptor. *EMBO J* 35: 1330–1345
- Perez-Reyes E, Castellano A, Kim HS, Bertrand P, Baggstrom E, Lacerda AE, Wei XY, Birnbaumer L (1992) Cloning and expression of a cardiac/brain beta subunit of the L-type calcium channel. *J Biol Chem* 267: 1792–1797
- Peterson BZ, DeMaria CD, Adelman JP, Yue DT (1999) Calmodulin is the Ca<sup>2+</sup> sensor for Ca<sup>2+</sup>-dependent inactivation of L-type calcium channels. *Neuron* 22: 549–558
- Qian H, Patriarchi T, Price JL, Matt L, Lee B, Nieves-Cintrón M, Buonarati OR, Chowdhury D, Nanou E, Nystoriak MA et al (2017) Phosphorylation of Ser1928 mediates the enhanced activity of the L-type Ca<sup>2+</sup> channel Cav1.2 by the beta2-adrenergic receptor in neurons. *Sci Signal* 10: eaaf9659
- Ran X, Miao HH, Sheu FS, Yang D (2003) Structural and dynamic characterization of a neuron-specific protein kinase C substrate, neurogranin. *Biochemistry* 42: 5143–5150
- Ribeiro Ede A Jr, Pinotsis N, Ghisleni A, Salmazo A, Konarev PV, Kostan J, Sjöblom B, Schreiner C, Polyansky AA, Gkougkoulia EA et al (2014) The structure and regulation of human muscle alpha-actinin. *Cell* 159: 1447–1460
- Sachs F, Neil J, Barkakati N (1982) The automated analysis of data from single ionic channels. *Pflugers Arch* 395: 331–340

- Schroder F, Handrock R, Beuckelmann DJ, Hirt S, Hullin R, Priebe L, Schwinger RH, Weil J, Herzig S (1998) Increased availability and open probability of single L-type calcium channels from failing compared with nonfailing human ventricle. *Circulation* 98: 969–976
- Schwieters CD, Kuszewski JJ, Tjandra N, Clore GM (2003) The Xplor-NIH NMR molecular structure determination package. *J Magn Reson* 160: 65–73
- Seisenberger C, Specht V, Welling A, Platzer J, Pfeifer A, Kuhbandner S, Striessnig J, Klugbauer N, Feil R, Hofmann F (2000) Functional embryonic cardiomyocytes after disruption of the L-type alpha1C (Cav1.2) calcium channel gene in the mouse. *J Biol Chem* 275: 39193–39199
- Sinnegger-Brauns MJ, Hetzenauer A, Huber IG, Renstrom E, Wietzorrek G, Berjukov S, Cavalli M, Walter D, Koschak A, Waldschutz R et al (2004) Isoform-specific regulation of mood behavior and pancreatic beta cell and cardiovascular function by L-type Ca<sup>2+</sup> channels. *J Clin Invest* 113: 1430–1439
- Splawski I, Timothy KW, Sharpe LM, Decher N, Kumar P, Bloise R, Napolitano C, Schwartz PJ, Joseph RM, Condouris K et al (2004) Ca<sub>v</sub>1.2 calcium channel dysfunction causes a multisystem disorder including arrhythmia and autism. *Cell* 119: 19–31
- Tjandra N, Bax A (1997) Direct measurement of distances and angles in biomolecules by NMR in a dilute liquid crystalline medium. *Science* 278: 1111–1114
- Tseng PY, Henderson PB, Hergarden AC, Patriarchi T, Coleman AM, Lillya MW, Montagut-Bordas C, Lee B, Hell JW, Horne MC (2017) alpha-Actinin promotes surface localization and current density of the Ca<sup>2+</sup> channel Ca<sub>v</sub>1.2 by binding to the IQ region of the alpha1 subunit. *Biochemistry* 56: 3669–3681
- Tuluc P, Molenda N, Schlick B, Obermair GJ, Flucher BE, Jurkat-Rott K (2009) A Ca<sub>v</sub>1.1 Ca<sup>2+</sup> channel splice variant with high conductance and voltage-sensitivity alters EC coupling in developing skeletal muscle. *Biophys J* 96: 35–44
- Turner M, Anderson DE, Rajan S, Hell JW, Ames JB (2016) Chemical shift assignments of the C-terminal EF-hand domain of alpha-actinin-1. *Biomol NMR Assign* 10: 219–222
- Van Petegem F, Chatelain FC, Minor DL Jr (2005) Insights into voltage-gated calcium channel regulation from the structure of the Ca<sub>v</sub>1.2 IQ domain-Ca<sup>2+</sup>/calmodulin complex. *Nat Struct Mol Biol* 12: 1108–1115
- Wingard JN, Chan J, Bosanac I, Haeseleer F, Palczewski K, Ikura M, Ames JB (2005) Structural analysis of Mg<sup>2+</sup> and Ca<sup>2+</sup> binding to CaBP1, a neuron-specific regulator of calcium channels. *J Biol Chem* 280: 37461–37470
- Wu X, Bers DM (2007) Free and bound intracellular calmodulin measurements in cardiac myocytes. *Cell Calcium* 41: 353–364
- Wyszynski M, Lin J, Rao A, Nigh E, Beggs AH, Craig AM, Sheng M (1997) Competitive binding of alpha-actinin and calmodulin to the NMDA receptor. *Nature* 385: 439–442
- Yang T, Xu X, Kernan T, Wu V, Colecraft HM (2010) Rem, a member of the R GK GTPases, inhibits recombinant Ca<sub>v</sub>1.2 channels using multiple mechanisms that require distinct conformations of the GTPase. *J Physiol* 588: 1665–1681
- Zamponi GW, Striessnig J, Koschak A, Dolphin AC (2015) The physiology, pathology, and pharmacology of voltage-gated calcium channels and their future therapeutic potential. *Pharmacol Rev* 67: 821–870
- Zhabotinsky AM, Camp RN, Epstein IR, Lisman JE (2006) Role of the neurogranin concentrated in spines in the induction of long-term potentiation. *J Neurosci* 26: 7337–7347
- Zhang Y, Li Z, Sacks DB, Ames JB (2012) Structural basis for Ca<sup>2+</sup>-induced activation and dimerization of estrogen receptor alpha by calmodulin. *J Biol Chem* 287: 9336–9344
- Zhang Y, Matt L, Patriarchi T, Malik ZA, Chowdhury D, Park DK, Renieri A, Ames JB, Hell JW (2014) Capping of the N-terminus of PSD-95 by calmodulin triggers its postsynaptic release. *EMBO J* 33: 1341–1353
- Zhong L, Kaleka KS, Gerges NZ (2011) Neurogranin phosphorylation fine-tunes long-term potentiation. *Eur J Neurosci* 33: 244–250
- Zuhlke RD, Pitt GS, Deisseroth K, Tsien RW, Reuter H (1999) Calmodulin supports both inactivation and facilitation of L-type calcium channels. *Nature* 399: 159–162
- van Zundert GC, Rodrigues JP, Trellet M, Schmitz C, Kastiris PL, Karaca E, Melquiond AS, van Dijk M, de Vries SJ, Bonvin AM (2016) The HADDOCK2.2 web server: user-friendly integrative modeling of biomolecular complexes. *J Mol Biol* 428: 720–725
- Zweckstetter M (2008) NMR: prediction of molecular alignment from structure using the PALES software. *Nat Protoc* 3: 679–690